Journal Pre-proof

Tail nerve electrical stimulation promoted the efficiency of transplanted spinal cord-like tissue as a neuronal relay to repair the motor function of rats with transected spinal cord injury

Bi-Qin Lai, Rong-Jie Wu, Wei-Tao Han, Yu-Rong Bai, Jia-Lin Liu, Hai-Yang Yu, Shang-Bin Yang, Lai-Jian Wang, Jia-Le Ren, Ying Ding, Ge Li, Xiang Zeng, Yuan-Huan Ma, Qi Quan, Ling-Yan Xing, Bin Jiang, Ya-Qiong Wang, Ling Zhang, Zheng-Hong Chen, Hong-Bo Zhang, Yuan-Feng Chen, Qiu-Jian Zheng, Yuan-Shan Zeng

PII: S0142-9612(23)00111-4

DOI: https://doi.org/10.1016/j.biomaterials.2023.122103

Reference: JBMT 122103

To appear in: *Biomaterials*

Received Date: 21 October 2022

Revised Date: 19 March 2023

Accepted Date: 23 March 2023

Please cite this article as: Lai B-Q, Wu R-J, Han W-T, Bai Y-R, Liu J-L, Yu H-Y, Yang S-B, Wang L-J, Ren J-L, Ding Y, Li G, Zeng X, Ma Y-H, Quan Q, Xing L-Y, Jiang B, Wang Y-Q, Zhang L, Chen Z-H, Zhang H-B, Chen Y-F, Zheng Q-J, Zeng Y-S, Tail nerve electrical stimulation promoted the efficiency of transplanted spinal cord-like tissue as a neuronal relay to repair the motor function of rats with transected spinal cord injury, *Biomaterials* (2023), doi: https://doi.org/10.1016/j.biomaterials.2023.122103.

Credit Author Statement

YSZ, **QJZ**, and **YFC** designed and supervised the study. **BQL**, **RJW**, **WTH**, **YRB**, **JLL**, **HYY**, **SBY**, **LJW**, **JLR**, and **YQW** performed the experiments and collected the data. **BQL**, **RJW**, **WTH**, and **YSZ** summarized, analyzed, and plotted the data and drafted the manuscript. **YD**, **GL**, **XZ**, **YHM**, **QQ**, **LYX**, **BJ**, **LZ**, and **ZHC** helped with study planning and critically reviewed the manuscript. **BQL**, **YSZ** and **RJW** wrote and finalized the article.

Tail nerve electrical stimulation promoted the efficiency of transplanted spinal cord-like tissue as a neuronal relay to repair the motor function of rats with transected spinal cord injury

Bi-Qin Lai[1,3,4,5,#], Rong-Jie Wu[2,12,#], Wei-Tao Han[3,#], Yu-Rong Bai[1], Jia-Lin Liu[1], Hai-Yang Yu[2], Shang-Bin Yang[1], Lai-Jian Wang[5], Jia-Le Ren[5], Ying Ding[1,3,5], Ge Li[7], Xiang Zeng[1,3,5], Yuan-Huan Ma[8], Qi Quan[9], Ling-Yan Xing[4], Bin Jiang[5], Ya-Qiong Wang[11], Ling Zhang[10], Zheng-Hong Chen[10], Hong-Bo Zhang[3], Yuan-Feng Chen[2,*], Qiu-Jian Zheng[2,*], Yuan-Shan Zeng[1,3,4,5,6,*]

[1]Key Laboratory for Stem Cells and Tissue Engineering, Sun Yat-sen University, Ministry of Education, Guangzhou 510080, China

[2]Department of Orthopedics, Guangdong Provincial People's Hospital (Guangdong Academy of Medical Sciences), Southern Medical University, Guangzhou 510100, China

[3]Co-innovation Center of Neuroregeneration, Nantong University, Nantong 226001, China

[4]Department of Histology and Embryology, Zhongshan School of Medicine, Sun Yat-sen University, Guangzhou 510080, China

[5]Guangdong Provincial Key Laboratory of Brain Function and Disease, Zhongshan School of Medicine, Sun Yat-sen University, Guangzhou 510080, China

[6]Institute of Spinal Cord Injury, Sun Yat-sen University, Guangzhou 510800, China

[7]Medical Research Center, Guangdong Cardiovascular Institute, Guangdong Provincial People's Hospital, Guangdong Academy of Medical Science, Guangzhou 510100, China

[8]Guangzhou Institute of Clinical Medicine, Guangzhou First People's Hospital, South China University of Technology, Guangzhou 510180, China

[9]Department of Orthopedic Surgery, Key Laboratory of Musculoskeletal Trauma & War Injuries PLA, Beijing Key Lab of Regenerative Medicine in Orthopedics, the 4th Medical Centre, Chinese PLA General Hospital, Beijing 100048, China

[10]Department of Geriatrics, The First Affiliated Hospital, Sun Yat-sen University, Guangzhou 510080, China

[11]Department of Electron Microscope, Zhongshan School of Medicine, Sun Yat-sen University, Guangzhou 510080, China

[12]Shantou University Medical College, Shantou 515041, China

[#]These authors contributed equally to this work.

Running title: Synergistic effect of TNES and SCLT in SCI repair

*Corresponding authors:
Yuan-Shan Zeng, M.D., Ph.D.
Department of Histology and Embryology
Zhongshan School of Medicine,
Sun Yat-sen University
74# Zhongshan 2nd Road, Guangzhou 510080, China
Tel: +86-20-87332698
Fax: +86-20-87332698
E-mail: zengysh@mail.sysu.edu.cn

Qiu-Jian Zheng, M.D.
Department of Orthopedics
Guangdong Provincial People's Hospital (Guangdong Academy of Medical Sciences),
Southern Medical University
Guangzhou 510100, China
E-mail: zhengqiujian@gdph.org.cn

Yuan-Feng Chen, M.D.
Department of Orthopedics
Guangdong Provincial People's Hospital (Guangdong Academy of Medical Sciences),
Southern Medical University
Guangzhou 510100, China
E-mail: chenyuanfeng@gdph.org.cn

ABSTRACT

Following transected spinal cord injury (SCI), there is a critical need to restore nerve conduction at the injury site and activate the silent neural circuits caudal to the injury to promote the recovery of voluntary movement. In this study, we generated a rat model of SCI, constructed neural stem cell (NSC)-derived spinal cord-like tissue (SCLT), and evaluated its ability to replace injured spinal cord and repair nerve conduction in the spinal cord as a neuronal relay. The lumbosacral spinal cord was further activated with tail nerve electrical stimulation (TNES) as a synergistic electrical stimulation to better receive the neural information transmitted by the SCLT. Next, we investigated the neuromodulatory mechanism underlying the action of TNES and its synergism with SCLT in SCI repair. TNES promoted the regeneration and remyelination of axons and increased the proportion of glutamatergic neurons in SCLT to transmit brain-derived neural information more efficiently to the caudal spinal cord. TNES also increased the innervation of motor neurons to hindlimb muscle and improved the microenvironment of muscle tissue, resulting in effective prevention of hindlimb muscle atrophy and enhanced muscle mitochondrial energy metabolism. Tracing of the neural circuits of the sciatic nerve and tail nerve identified the mechanisms responsible for the synergistic effects of SCLT transplantation and TNES in activating central pattern generator (CPG) neural circuits and promoting voluntary motor function recovery in rats. The combination of SCLT and TNES is expected to provide a new breakthrough for patients with SCI to restore voluntary movement and control their muscles.

Keywords: Synergistic electrical stimulation; Spinal cord-like tissue; Transplantation; Transected spinal cord injury; Voluntary motor function recovery

1. Introduction

A transected spinal cord injury (SCI) may induce the loss of innervation from the brain to the spinal cord below the injury, resulting in functional silence. Spinal epidural electrical stimulation (EES) of a functionally silent spinal neural network at the caudal end of the injury can contribute to the restoration of motor function in patients with paralysis [1, 2]. However, the recovery of voluntary motor function depends on repairing the spinal cord relay of brain-derived neural signals at the SCI site [1, 3, 4]. If the repair of nerve conduction in the injured spinal cord is maximized, and the spinal cord neural circuit is re-activated, it is expected that the synergism between treatments results in greater recovery of voluntary motor function.

In addition to improving the microenvironment of the SCI site to improve the regenerative potential of axons, the key to repairing post-SCI voluntary motor function lies in: 1) supplementing donor neurons and promoting regeneration of host axons to form functional synaptic connections between them to realize the retransmission of brain neural information to targeted neurons below the level of the injury [5, 6]; 2) replenishing oligodendrocytes to promote the myelination of regenerated axons to transmit neural information stably and efficiently [7-9]; 3) activating the injured caudal spinal cord neural circuit to promote functional integration of new and caudal spinal cord neurons [4, 10]; and 4) enhancing muscle innervation to prevent skeletal muscle atrophy of paralyzed limbs [11, 12].

At present, there is a significant lack of suitable methods to simultaneously induce stem cells into neurons or myelinating cells at the site of SCI [13, 14]. Previous research has shown that re-inducing stem cells into neurons or myelinating cells *in vitro* can alleviate the effects of the microenvironment on the uncertain fate of differentiating stem cells *in vivo* [7, 15]. Studies have also shown that the neural network tissue constructed by tissue engineering can not only provide

neurons and myelinating cells to the SCI site but also better exerts effect on the injury microenvironment and maintains the survival and differentiation phenotype of transplanted cells to achieve functional integration with the spinal cord [7, 16, 17]. Advancements in tissue engineering or three-dimensional (3D) printing is expected to simulate cell composition and tissue structure in the spinal cord and create a more efficient neuronal relay than that created by the traditional 3D culture [17-20].

Hence, we used the strategy of modular construction and programmed assembly to simulate the white and gray matter of spinal cord to combat the adverse injury microenvironment and relay neural information more efficiently [7]. Specifically, we co-cultivated and assembled white matter-like tissue (WMLT) mainly comprising oligodendrocytes that overexpressed ciliary neurotrophic factor (CNTF) and gray matter-like tissue (GMLT) mainly comprising neurons that overexpressed neurotrophin-3 (NT-3) and NT-3-specific receptor tyrosine protein kinase C (TrkC) into spinal cord-like tissue (SCLT). CNTF and NT-3 had positive effects on the axon regeneration, the survival of transplanted cells, and the formation of myelin sheaths by oligodendrocytes [8, 9]. The SCLT was transplanted into a rat model of spinal cord transection to allow us to determine whether behavioral recovery was achieved due to collateral sprouting from neighbor uninjured axons or due to the transmission of neural information following the integration of regenerated axons with transplanted neurons. Nonetheless, it may take 2-6 months for the transplanted SCLT to fully achieve functional integration with the spinal cord [5]. In the meantime, neural circuits below the SCI level are functionally silent, with injured neuronal apoptosis and muscular apraxia atrophy beforehand, which all restrict the functional integration of SCLT with caudal spinal cord neural circuits and influence the repair of motor function [6, 7, 21, 22].

Recent research has suggested that performing modulated medium frequency tail nerve electrical stimulation (TNES) in rats with SCI effectively protects injured L1–L5 spinal cord neurons and prevents hindlimb muscle atrophy. However, no significant recovery of motor function in rats with SCI was observed after TNES when compared to SCI rats without any intervention [12]. This may be related to the less efficient transmission of brain-derived neural information to spinal cord neurons below the site of SCI. However, the studies focusing on the neural circuits related to TNES and the mechanisms are relatively scarce.

To solve these scientific problems, the present study aimed to investigate whether a new strategy of SCLT transplantation combined with TNES can promote the repair and functional activation of neural circuits and reveal whether the two approaches synergize in a novel mechanism to promote significant recovery of voluntary motor function.

2. Materials and methods

2.1. Isolation, culture, and induction of NSCs

NSCs were isolated from GFP transgenic Sprague-Dawley (SD) rats (Osaka University, Osaka, Japan), as described previously [16]. Briefly, cells obtained from the hippocampus were cultured in Dulbecco's modified Eagle medium (DMEM)/F12 (1:1) containing 1× B27 (Life Technologies, Gaithersburg, MD, USA) and 20 ng/mL basic fibroblast growth factor (bFGF, Life Technologies) and grown as neurospheres in suspension. Nestin immunoreactivity was confirmed for all neurospheres. Oligodendrocyte precursor cells (OPCs) were obtained according to the protocols published previously [7]. Briefly, NSCs were cultured with DMEM/F12 containing 10 ng/mL bFGF, 10 ng/mL platelet-derived growth factor AA (Supplementary-AA, Life Technologies) and 30 ng/mL triiodothyronine (T3, Sigma–Aldrich, St. Louis, MO,USA) for 5

days. The OPCs were tested for the expression of neuron-glia antigen 2 (NG2) and A2B5 (a marker for OPCs). A summary of antibodies used is provided in Supplementary Table 1.

2.2. Genetic modification of NSCs and construction of SCLT

NSCs were transfected using an adeno-associated virus (AAV) vector (Vigene Biosciences, Rockville, MD, USA) carrying the NT-3 coding sequence (NM_002527, pAV-CMV-NT-3-P2A-GFP, Vigene Biosciences) or its receptor TrkC (NM_001007156, pAV-CMV-TrkC-P2A-GFP, Vigene Biosciences) gene. For OPC transfection, the CNTF gene was delivered via AAV (NM_000614 pAV-CMV-CNTF-P2A-GFP, Vigene Biosciences).

The SCLT was constructed as described previously [7]. Briefly, for the GMLT construction, a mixed cell suspension in 20 μL containing equal amounts of NT-3-NSCs and TrkC-NSCs (2×10^5 cells for each scaffold) was dripped into the pre-wetted collagen sponge scaffold (2 mm in diameter and 2 mm in length) and the scaffold was cultured in neural basal medium containing 1% fetal bovine serum (FBS). For WMLT construction, a total of 2×10^5 CNTF-OPCs in 20 μL culture medium were seeded to the collagen sponge ring (3 mm in outer diameter, 2 mm in inner diameter, and 2 mm in length) and the scaffold was cultured in DMEM/F12 containing 10 ng/mL bFGF, 10 ng/mL PDGF-AA, 30 ng/mL T3, and 1% FBS. The GMLT and WMLT modules were cultured separately for 7 days before they were assembled into the SCLT. The SCLT was maintained in DMEM/F12 (1:1) with 1× B27 supplement and 5% FBS for another 7 days.

2.3. Whole-cell recordings

The whole-cell recordings was applied to confirm the neuronal function of the SCLT using an Integrated Patch-Clamp Amplifier (Sutter Instrument, Novato, CA, USA) controlled by Igor 7

software (WaveMetrics, Portland, OR, USA) filtered at 5 kHz and sampled at 10 kHz. Igor 7 software was also used for acquisition and analysis. The external solution (ACSF) contained 140 mM NaCl, 5 mM KCl, 2 mM $CaCl_2$, 1 mM $MgCl_2$, 10 mM 4-(2-hydroxyethyl)-1-piperazineethanesulfonic acid (HEPES), and 10 mM glucose (290-300 mOsm, pH adjusted to 7.3). For inducing action potential, whole-cell recordings were performed in current-clamp mode at –60 mV. Patch pipettes (2–4 mΩ) were filled with the internal solution consisting of the following (in mM): 130 K-gluconate, 10 KCl, 10 HEPES, 0.5 Na_3GTP, 4 MgATP, 10 Na-phosphocreatine, and 0.2% biocytin, pH 7.2–7.4. The osmolarity was 275–290 mOsm. Spikes were induced by incrementally increasing the current injection (each step increase was 50 pA). To isolate AMPAR-mediated mEPSCs from neurons in SCLT, 1 μM TTX, 20 μM bicuculline, and 100 μM D,L-APV were added to the ACSF (2 mL/min) which was continually bubbled with 95% O_2/5% CO_2. mEPSCs were recorded at a holding potential (Vh) of –70 mV. To isolate GABA receptor-mediated mIPSCs from neurons in SCLT, 1 μM TTX, 20 μM CNQX, and 100 μM D,L-APV were added to the ACSF. mIPSCs were recorded at a holding potential (Vh) of –60 mV as inward current with the Cs-based internal solution consisting of the following (in mM): 120 CsCl, 8 NaCl, 2 EGTA, 10 HEPES, 5 QX-314, 4 ATP, 10 Na-phosphocreatine and 0.5 GTP, pH 7.4, at 270–290 mOsm.

2.4. Dynamic assessment of glutamate release

The glutamate sensor intensity-based glutamate-sensing fluorescent reporter (iGluSnFR) was used as described previously [23]. Briefly, SCLT was transfected with AAV2/1.hSynapsin1.SF-iGluSnFR.S72A (Brain VTA, Wuhan, China) *in vitro* and used for experiments after 14 days. iGluSnFR was used to evaluate synaptic glutamate release after glutamate or high [K^+] stimulation.

Neuropharmacological drugs (100 mM glutamate, 50 mM KCl, and 1 mM TTX) were delivered with perfusion and kept for a 10 min incubation time before washing out. Changes in fluorescence intensity of iGluSnFR were captured with a LSM780 confocal laser scanning system (Zeiss, Germany). Regions of interest (ROIs) were manually selected and the mean fluorescence for each ROI was calculated at each time frame. A control experiment to assess nonspecific bleaching of fluorescence was performed simultaneously.

2.5. Surgery and SCLT transplantation

All experimental protocols and animal handling procedures were approved by the Animal Care and Use Committee of Sun Yat-sen University and were consistent with the National Institutes of Health Guide for the Care and Use of Laboratory Animals. Three days before surgery, animals were given cyclosporine A by subcutaneous injections. All surgical procedures were performed under sterile conditions in a designated animal surgery area. Adult female SD rats (220–250 g, supplied by the Experimental Animal Center of Sun Yat-sen University) were anesthetized. The skin and muscles were cut through to expose the laminae. The laminae at the T9-T10 vertebral level were carefully removed with biting forceps to expose a length of approximately 6 mm of spinal cord. The dura mater was opened with curved iris scissors and the T10 segment of spinal cord was transected vertically with straight iris scissors. A cylindrical piece of spinal cord (2 mm in length) was removed, and a cylindrical piece of SCLT of the same length was implanted after adequate hemostasis. The exposed spinal cord without dura mater was covered with a thin sheet of collagen sponge so that it was separated from the connective tissue, and then the muscle, fascia, and skin, were sutured layer by layer. In the SCI group, we removed a piece of spinal cord (2 mm in length) but did not graft a collagen sponge scaffold into the cavity. After adequate hemostasis,

the exposed spinal cord was covered with a thin sheet of collagen sponge to replace the dura mater; then, we sutured the muscle, fascia, and skin in a sequential manner. All rats received extensive post-surgery care including intramuscular injection of penicillin (50,000 U/kg/d) for 7 days and manual emiction twice daily before voluntary micturition function was reestablished. Cyclosporine A was administrated once daily for 2 months.

2.6. TNES intervention

TNES was performed on SCI or SCLT rats (the E-SCI and E-SCLT groups) according to the protocol reported previously [12]. Surgeons performing the animal surgery were uninformed about whether animals were included in the TNES treatment group (the E-SCI and E-SCLT groups) or the non-TNES treatment group (the SCI and SCLT groups). On the 8th day after surgery, the animals were considered to pass critical periods postoperatively and those with stable vital signs were randomly grouped by the technicians. TNES therapy was commenced on the 8th day after surgery and was administered five times a week for 8 weeks. To perform TNES, each rat was kept in an open field (a square box that was 1 m in length) to permit free movement. Two electrodes were then placed 1 cm apart (to avoid a short circuit) on the base of the tail and connected to a physical therapy instrument (Type J18A1Quan-Ri-Kang Company, Shenzhen, China). The stimulation strength was adjusted to 20 mA at a frequency of 4 kHz to induce a slight vibration of the tail or a twitch of the hindlimbs, and each treatment lasted for 20 min.

2.7. Assessment of locomotor function

During the 1st week after surgery, we observed the behavior of the animals. Rats with BBB scores greater than 3, with hindlimb spasticity, or with sensory abnormalities such as hindlimb

biting, were excluded from the experiment. Follow-up functional scoring was performed by technicians outside of surgery and TNES treatment was performed according to established criteria in a double-blind manner. Rat hindlimb function was assessed weekly after surgery with the BBB open-field locomotor test [24], glass cube locomotor function observation (each rat was placed in a glass cube that was 30 cm in height) and inclined grid climbing test [7, 25]. The BBB test was used to quantitatively evaluate voluntary movements and body weight support capability. Hindlimb standing capability was generally assessed by observing rat locomotion in the glass cube. The modified grid climbing test was used to detect the spontaneous placing reflex triggered by direct (light and heavy) contact between the dorsal surface of the foot and the grid frame [25]. This test can well reflect the degree of sensory and motor function recovery of the paralytic hindlimbs. The number of foot grasping was counted when each rat grasped the grid frame with the hindlimb feet at 8 weeks after TNES treatment [25].

2.8. Neural pathway tracing

Rats were anesthetized with 1% pentobarbital sodium (40 mg/kg) 8 weeks after TNES. A longitudinal incision was made in the skin over the upper posterior part of the thigh and gluteal region. The gluteus maximus muscle was separated with a pair of iris scissors along the direction of its fibers to maximally expose the sciatic nerve. To minimize animal suffering, 2% lidocaine was applied with a cotton swab. The sciatic nerve was lightly crushed with a pair of blunt forceps before the injection to maximize tracer contact with nerve fibers. Under the guidance of a Leica MZ6 dissecting stereomicroscope (Leica Microsystems, Inc., Germany), the needle tip of a glass micropipette was advanced approximately 10 mm into the common peroneal component of the nerve and withdrawn 2–3 mm to make a potential pool for injection. One microliter 3% fluorogold

(FG, Fluorochrome, Denver, CO, USA) or pseudorabies virus (PRV, 2.5×10^9 PFU/ml, Brain VTA, China) was slowly injected over approximately 20 s. The needle tip was left in place for 3–4 min and was withdrawn slowly over 15–20 s to prevent leakage of the tracer. After injection, the injection site surface was washed with a saline-soaked cotton swab, and each nerve was ligated between the sites of inoculation and penetration of the epineurium with the micropipette. The wound was then sutured. Rats were prophylactically treated with ampicillin (100 mg/kg). For tail nerve tracing, 2 μL 2% cholera toxin B (CTB) conjugated to Alexa Fluor 555 (C-34779, Molecular Probes, Eugene, OR,USA) or 2.5 μL PRV (2.5×10^9 PFU/ml) was slowly injected into the tail in multiple subcutaneous injections (0.1 μL per injection site). Animals were sacrificed 7 days later.

2.9. Electrophysiological analysis

Before perfusion, electrophysiology (EP) was recorded as described previously to assess the functional status of motor signal conduction [7]. Briefly, following general anesthesia and exposure of the sciatic nerves and sensorimotor cortex (SMC), electrodes (NeuroExam M-800 Data Acquisition Analysis System, MEDCOM, Zhuhai, China) were connected to the sciatic nerve and SMC. CMEPs were recorded on the data acquisition analysis system.

2.10. Muscle atrophy analysis

All rats were deeply anesthetized with 1% pentobarbital sodium (50 mg/kg, i.p.) and systemically perfused with 0.9% NaCl containing 0.002% $NaNO_2$ and 0.002% heparin, followed with 4% paraformaldehyde. After perfusion, tissue was post fixed overnight in the same fixative. Tissue was then placed in 30% sucrose/phosphate buffered saline (PBS). Sections of selected spinal cord segments were cut at a 25-μm thickness using a cryostat. All sections were stored at

−30°C until further processing. Rats were sacrificed with overdose of anesthesia for detection of the wet weight of the gastrocnemius and tibialis anterior. The muscle tendons were carefully cut and the wet muscles were weighed using an electronic analytical balance with an accuracy of 0.1 mg.

2.11. Western blot analysis

Protein was extracted from lumbar spinal cord and the gastrocnemius muscle of each rat. Equal amounts of proteins were loaded onto a 10% polyacrylamide gel. Proteins were separated with electrophoresis, followed by being transferred to a polyvinylidene fluoride (PVDF) membrane. The membrane was incubated with primary antibodies at 4°C overnight, followed by being incubated with horseradish peroxidase (HRP)-conjugated secondary antibodies. The bands were detected with an enhanced chemiluminescence (ECL) western blotting substrate kit. The amount of glyceraldehyde 3-phosphate dehydrogenase (GAPDH) protein or heat shock protein 90 (HSP90) was used as loading control. A summary of antibodies used is provided in Supplementary Table 1.

2.12. Immunocytochemistry analyses

Specific proteins were detected using immunocytochemistry staining as described in previous publications. Briefly, sections were incubated with primary antibodies in 0.01 M PBS containing 0.3% Triton X-100 at 4°C overnight, followed by being incubated with secondary antibodies. The slides were then examined with a fluorescence microscope. A summary of antibodies used is provided in Supplementary Table 1.

2.13. Ultrastructure analyses

For SEM, SCLT was washed three times with PBS, fixed in 2.5% glutaraldehyde for 90 min, dehydrated with a series of graded ethanol solutions (70, 80, 90, 95, 100%), and freeze-dried for 2 days. The dried samples were coated with gold and examined with a scanning electron microscope (SEM, Philips XL30 FEG, Amsterdam, Netherlands).

For transmission electron microscopy (TEM), SCLT was fixed with 2.5% glutaraldehyde at 4°C for 1 h and postfixed with 1% osmic acid for 1 h. The tissue was dehydrated with graded ethanol solutions and embedded in Epon812 overnight, followed by polymerization at 60°C for 48 h. Ultrathin sections (100 nm thickness) were cut, double stained with lead citrate and uranyl acetate, and examined with an electron microscope (Philips CM 10).

For IEM, rats were transcardially perfused with 0.1 M of PBS containing 187.5 unit heparin per 100 mL, followed by perfusion with 4% paraformaldehyde, 0.1% glutaraldehyde, and 15% saturated picric acid. The dissected spinal cord was postfixed overnight at 4°C in fresh fixative and subsequently cut into 50-μm sagittal sections on a vibratome. To improve the penetration of antibodies, vibratome sections were transferred into cryoprotectant solution containing 25% sucrose and 10% glycerol in 0.1 M PBS overnight at 4°C, followed by a quick freeze-thaw in liquid nitrogen three times. After being washed with PBS, the sections were treated for 1 h with 20% goat serum (Tris buffer, pH 7.4) to block nonspecific binding of the antibody. Sections were incubated with primary antibodies (anti-GFP combined with anti-vesicular glutamate transporters 1 [VGluT1] or anti-PRV, $n = 3$) in 2% normal goat serum solution at 4°C for 24 h, incubated with secondary antibodies overnight at 4°C, and postfixed in 1% glutaraldehyde for 10 min. The antibody binding sections were detected by SABC-DAB Kit and gold enhanced with Gold EnhanceTM EM Plus Kit (NanoProbe 2114, USA), osmicated, dehydrated, and embedded in

Epon812. The Epon blocks were sectioned and examined with an electron microscope (Philips CM 10). A summary of antibodies used is provided in Supplementary Table 1.

2.14. Morphological quantification

For *in vivo* quantification of neurofilament $(NF)^+$ axons and myelin basic protein $(MBP)^+$ myelin sheaths, we selected areas that were within 2 mm rostral or caudal of the injury/graft site or 2 mm within the injury/graft site of each of the horizontal sections. One in every five sections from each animal was processed; a total of four sections per rat were analyzed (n = 5 in each group). NF^+ axons and MBP^+ myelin sheaths were converted to an area of interest (AOI) and the pixel area of each AOI was calculated by Image J software. The area of staining in each image was then determined as the proportion of stained pixels of the total number of pixels in each image that excluded cavity areas. For *in vivo* quantification of activity-regulated cytoskeleton-associated protein $(Arc)^+$ cells, one in every five sections from each animal was processed; a total of three sections per rat were analyzed (n = 5 in each group). The percentage of the Arc^+ area was calculated as per the quantification of NF^+ axons above. For quantification of paired box gene 7 protein $(Pax7)^+$, microtubule-associated protein 2 $(Map2)^+$, PRV^+, $VGluT1^+$, or glutamic acid decarboxylase 67 $(GAD67)^+$ cells, the percentage of immunopositive cells was calculated by counting the total number of immunopositive cells in the selected fields. The percentage of $Map2^+$ cells was obtained by the immunopositive cells divided by the total number of GFP^+ cells. For quantification of the percentage of $VGluT1^+$ or $GAD67^+$ cells, the immunopositive cells were calculated and the value obtained was then divided by the total number of $Map2^+$ cells. For quantification of $VGluT1^+$ nerve fibers, immunopositive nerve fibers with a length greater than 20

μm in the selected fields were counted. For quantification of innervated motor endplates, SYP^+ motor endplates were divided by the total number of motor endplates in the selected fields.

2.15. Statistical analysis

All statistical analyses were performed using the statistical software SPSS13.0. Data were presented as means ± standard deviation. When three sets of data were compared, one-way analysis of variance (ANOVA) with a least significant difference (LSD)-t (equal variance assumed) or Dunnett's T3 (equal variance not assumed) was performed. A statistically significant difference was accepted at $P < 0.05$.

3. Results

3.1. Modular assembly of SCLT

The WMLT and GMLT were constructed via gene modification and the 3D culture technique. To construct the WMLT module, the nestin-positive ($Nestin^+$) NSCs (Fig. 1a) were induced to become OPCs utilizing exogenous triiodothyronine (T3) and PDGF. Immunocytochemical analysis revealed high purity expression of the OPC marker neuroglycan 2 (NG2) and A2B5 in the induced cells (Fig. 1b). OPCs were transfected with adeno-associated viral (AAV)-CNTF, and were found to successfully co-express CNTF and oligodendrocyte transcription factor 2 (Olig2) after transfection (Fig. 1c). CNTF gene-modified OPCs were seeded into the collagen sponge ring to construct the WMLT module, followed by culturing for 7 days to promote WMLT maturation (Fig. 1d). Regarding the GMLT module, $Nestin^+$ NSCs transfected with an equal amount of AAV-NT-3 or AAV-TrkC were seeded in the collagen sponge column and then the expression of NT-3 and TrkC was confirmed with immunocytochemical analysis (Fig. 1e). Next, we investigated

hematoxylin and eosin (H&E)-stained sections which were sampled from the center of a series of WMLT (Fig. 1d) and GMLT (Fig. 1f) transverse sections before assembly. The results showed that the population of cells was dense in both modules (Fig. 1d and f). After 7 days of being cultured separately, WMLT and GMLT were assembled with SCLT for 7 days of co-culture (Fig. 1g).

Following 14 days of culture *in vitro*, the assembled SCLT roughly simulated the anatomical partitions of a spinal cord with no visible gap between the two modules (Fig. 1g and h). Few cells seeded in each module migrated to another part, as evidenced by the vast most majority of cells expressing MBP remaining in the outer ring imitating white matter (Fig. 1g), whereas green fluorescent protein $(GFP)^+$ cells remained in the core (Fig. 1g). Scanning electron microscopy (SEM) was performed to acquire the surface view of the SCLT (Fig. 1h). Examination at higher magnifications further revealed that the cells within the GMLT were extensively interconnected (Fig. 1i, arrows). In addition, many cell processes were observed in the WMLT (Fig. 1j, arrows).

3.2. Differentiation and functional maturation of NSCs in SCLT

Following the assembly of SCLT, over 80% of the NSCs differentiated into $Olig2^+$ cells (arrows); the remaining cells differentiated into glial fibrillary acidic protein-positive ($GFAP^+$) cells (arrowheads) in the WMLT (Fig. 1k). Some nerve fibers (arrowheads) grew into the region enriched in MBP^+ cells (Fig. 1l, arrows). Most differentiated cells in the GMLT expressed the neuronal marker Map2 (arrows), whereas few cells expressed the astrocyte marker GFAP (Fig. 1m, arrowheads). The VGluT1 (arrowheads) and inhibitory neurotransmitter enzyme GAD67 (arrow) were detected in $Map2^+$ neurons (Fig. 1n and o, arrows) in GMLT, illustrating that the cells differentiated into different subtypes with distinct function after neuronal induction. Some

neurons also highly expressed postsynaptic density protein 95 (PSD95, arrow) and synaptophysin (SYP, arrowheads) in the GMLT region (Fig. 1p), suggesting synaptic connections were well established between SCLT neurons. Electron microscopy further confirmed that neurons in the 14-day SCLT had made contact with neighboring cells and had built synaptic connections (Fig. 1q). Features of mature synapses, including synaptic vesicles (arrowheads) at the axon terminals, the formation of postsynaptic density (arrows), and membrane thickening, were observed at higher magnification (Fig. 1r and s). Multilayered myelin sheaths were observed to wrap an axon (asterisk) in the WMLT of the assembled SCLT (Fig. 1t).

Whole-cell recordings were performed to confirm the neuronal function of the SCLT. Action potential and synaptic transmission were measured in differentiated SCLT neurons. Action potentials induced by two different current injections were recorded (Fig. 1u), miniature excitatory postsynaptic currents (mEPSCs, Fig. 1v) and miniature inhibitory postsynaptic currents (mIPSCs, Fig. 1w) were detected in neurons in the SCLT cultured for 14 days, suggesting that differentiated SCLT neurons were mature and formed the excitatory and inhibitory neural networks. To visualize the dynamic release of glutamate in the SCLT, we performed the glutamate sensor iGluSnFR technique. Excitatory glutamate or high [K^+] stimulation evoked glutamate release in the GMLT in assembled SCLT as evidenced by dynamic fluorescence changes (Fig. 1x and Supplementary Video 1), and this effect was blocked with tetrodotoxin (TTX) (Supplementary Fig. 1).

3.3. Analyses of behavior, muscle wet weight, and electrophysiology

A 2-mm spinal cord segment was removed from the site of complete spinal cord transection at T10, resulting in complete hindlimb paralysis (Fig. 2a). SCLT was then transplanted within the gap created by injury. TNES began 8 days after surgery and transplantation, and performed five times a week for 8 weeks. Rats did not display any signs of distress, such as significant body

weight loss, aggression, or vocalization when touched, or porphyrin staining following the TNES intervention and SCLT transplantation during the 8 weeks of observation. The open-field locomotor, inclined grid climbing, and glass cube tests were performed on the E-SCI, SCLT, and E-SCLT groups (Fig. 2b–d, arrows showing paralyzed hindlimbs, Supplementary Video 2). Starting 3 weeks post SCI, small improvements in hindlimb function were observed in the SCLT and E-SCLT groups. Eight weeks post SCI, significant improvements in hindlimb function were observed in the E-SCI and SCLT groups when better hindlimb motor function was restored in the E-SCLT groups compared to that in rats receiving individual treatments.

Rats in the SCI group showed no spontaneous placing reflex; instead, they climbed the inclined grid using the forelimbs, dragging their hindlimbs and falling frequently (Supplementary Video 3). In contrast, rats receiving TNES or SCLT implants had more obvious hindlimb placing reflexes, with TNES and SCLT implant-treated rats demonstrating the strongest placing (Supplementary Video 3). The quantification result showed that the number of foot grasping in the E-SCLT group was significantly more than that in the SCLT group (Supplementary Fig. 2), suggesting that the rats in the E-SCLT group have significant sensory and motor function recovery of the hindlimbs. Rats in the E-SCLT groups supported their body weights with their hindlimbs during the immobile posture, thus showing that more muscle strength was preserved when rats were treated with the combination of TNES and SCLT (Fig. 2d). We observed less atrophy of the gastrocnemius and tibialis anterior in rats receiving TNES for 8 weeks (Fig. 2e).

The average Basso, Beattie, and Bresnahan (BBB) score was 9.7 in the E-SCLT group (n = 8 in each group), indicating that treated rats could move all three joints with weight-supported stepping of the hindlimbs. Rats in the SCLT group (with average BBB scores of 8.7) could move all three joints of the hindlimbs extensively but with rare weight-supported stepping (Fig. 2f). The

wet weights of the gastrocnemius and tibialis anterior muscle in the E-SCI and E-SCLT groups were higher than those in rats from the SCI and SCLT groups 8 weeks postoperatively, indicating that TNES is a potential strategy to alleviate hindlimb muscle atrophy after SCI (Fig. 2g). To confirm the restoration of function in SCI rats, latency and amplitude of cortical motor evoked potentials (CMEPs) were evaluated to reflect the conduction velocity and number of axons involved in the monitored neural pathways. Rats in the SCI group had negligible CMEP signal levels, in sharp contrast to those in the normal (Nor) group. The rats in the E-SCLT group had the highest CMEP amplitudes; the latency was shorter in the SCLT and E-SCLT groups than that in the SCI and E-SCI groups (Fig. 2j). This observation plus the change of CMEP curve patterns in the SCLT and E-SCLT groups suggested that CMEP signals may be relayed by the SCLT implants, and TNES treatment further enhanced the reconstruction of motor pathways.

3.4. Regeneration of nerve fibers and myelination in the injury/graft site

Transplanted SCLT integrated well with the spinal cord, as evidenced by no gaps remaining between the implant and host tissue (Fig. 3a). In the SCLT group, MBP^+ cells in the WMLT maintained their phenotypes *in vivo* after transplantation (Fig. 3a and b). Like the neurotransmitter profile in the GMLT *in vitro*, $Map2^+$ neurons at the injury/graft site epicenter expressed VGluT1 or GAD67 (Fig. 3c and d). More nerve fibers co-expressing GFP and NF were observed in the injury/graft site, and more were wrapped with MBP^+ cells in the E-SCLT groups than those in the SCLT groups (Fig. 3e and f). Nerve fiber growth and myelination in the injury site were improved after TNES treatment in the E-SCI group (Supplementary Fig. 3). Immunocytochemical staining showed that more donor cells differentiated into $VGluT1^+$ neurons in the injury/graft site in the E-SCLT group than those in the SCLT group (Fig. 3g and h, see statistical results below).

To further quantify nerve fiber growth and myelination, we measured the fluorescence intensity of nerve fibers and myelinating cells in the regions rostral and caudal to/in the injury/graft site of spinal cord. The relative densities of NF^+ nerve fibers and MBP^+ myelinating cells in the E-SCI and SCLT groups were higher than those in the SCI group (Fig. 3i). The relative density of NF^+ nerve fibers and MBP^+ myelinating cells was enhanced following the combination of TNES and SCLT (Fig. 3i). Overall, the WMLT component of the SCLT implants in TNES-treated animals led to the more efficient formation of myelin sheaths on nerve fibers in the injury/graft site, thus resembling white matter in the normal spinal cord. Although there was no significant difference in the number of $Map2^+$ neurons between the SCLT and E-SCLT groups, the proportion of $VGluT1^+$ neurons was significantly higher, and the proportion of $GAD67^+$ neurons was significantly lower in the E-SCLT group (Fig. 3j).

3.5. Analyses of neuronal activation-related proteins in lumbar spinal cord

To determine the effect of TNES on neurons in the lumbar spinal cord, we compared proteins relevant to neuronal activation in L2 and L5 spinal cord transverse sections between the SCLT and E-SCLT groups. Activity-regulated cytoskeleton-associated protein (Arc, a marker of synaptic plasticity of neurons) was uniformly distributed in the spinal cord anterior and posterior horns (Fig. 4a–d). Arc expression was higher at the spinal cord L2 and L5 segments in the E-SCLT group compared with the SCLT group (Fig. 4b and d, see statistical results below). c-Fos (immediate-early gene protein product in activated neurons) was expressed at high levels in the L2 and L5 segments of the spinal cord in the E-SCLT group but was not detected in the SCLT group (Fig. 4e). C-Fos expression was also detected in $VGluT1^+$ neurons in the L1 dorsal nucleus of the spinal cord, suggesting that TNES activated ascending neural pathways (Supplementary Fig. 4). Donor

neurons labeled with c-Fos/Map2/GFP were observed in the injury/graft site in the E-SCLT group (Fig. 4g). Quantitation of the immunocytochemical staining revealed that the relative density of Arc^+ cells in the L2 and L5 segments in the E-SCLT group was higher than that in the SCLT group (Fig. 4h).

To further evaluate synaptic plasticity-related proteins associated with TNES, we performed a western blot test with tissues acquired from the spinal cord lumbar segment in all groups. NT-3 levels were significantly higher in the E-SCLT group than those in the SCLT group, and lower in the SCI and E-SCI group than those in the SCLT and E-SCLT groups, whereas no significant differences in those in the E-SCI and SCI groups were detected (Fig. 4i and j). Immunocytochemical staining indicated that NT-3 was located in neurons in the lumbar spinal cord (L2 and L5) in the E-SCLT group (Supplementary Fig. 5). The increased NT-3 was associated with an increased probability of GFP^+ neurons within the graft to form neo-connections with host neurons (Supplementary Fig. 6).

Other synaptic proteins, including SYP and PSD95, were significantly lower in the SCI group than those in the Nor group. SYP and PSD95 levels in the E-SCLT group were discernibly different (to varying degrees) from those in the E-SCI and SCLT groups, which were nearly comparable to those in the Nor group (Fig. 4i and j). Thus, TNES and SCLT transplantation increased the expression levels of SYP and PSD. Moreover, the levels of choline acetyltransferase (ChAT, a protein of excitatory neurons and their synapses) were significantly higher in the E-SCLT group than those in the SCLT group.

3.6. Regeneration of $VGluT1^+$ nerve fibers and integration of the SCLT implant with host tissue

Because excitatory neurotransmission is related to motor function, we analyzed changes in glutaminergic nerve fibers with immunocytochemical staining. In the SCLT group, regenerated VGluT1$^+$ nerve fibers were distributed to regions rostral and caudal to/in the graft site (Fig. 5a and a1–a3). More regenerated VGluT1$^+$ nerve fibers distributed to regions rostral and caudal to/in the injury/graft site in the E-SCLT group than in the SCLT group (Fig. 5b and b1–b3). VGluT1$^+$ nerve fibers were in direct contact with GFP$^+$ neurons in the injury/graft site in the E-SCLT group (Fig. 5c) and those with a length of more than 20 μm were counted in the regions rostral and caudal to/in the injury/graft site. There were more VGluT1$^+$ nerve fibers in the caudal region to/in the injury/graft site in the E-SCI, SCLT, and E-SCLT groups than in the SCI group (Fig. 5d). No statistical difference was detected in the number of VGluT1$^+$ nerve fibers in the rostral region to the injury/graft site in the SCLT and E-SCLT groups. However, they were significantly more numerous than those in the SCI and E-SCI groups (Fig. 5d), suggesting that SCLT transplantation combined with TNES promotes regeneration of VGluT1$^+$ nerve fibers in injured spinal cord. Double labeling immunoelectron microscopy (IEM) in the E-SCLT group revealed a synapse-like structure (Fig. 5e) between the VGluT1$^+$ nerve fibers (diaminobenzidine [DAB] staining) and GFP$^+$ neurons (nanogold particle staining). In the injury/graft site, numerous round vesicles (arrowheads) were seen in the axoplasm on one side of the junction (i.e., the presynaptic terminal) next to the postsynaptic densities (a thick zone), characteristics of excitatory nonsymmetric synapses (Type-I synapses) (Fig. 5e1).

To validate our hypothesis that the combination of TNES with SCLT more effectively relayed descending neural signals from the region rostral to the injury/graft site and subsequently transmitted information to the caudal spinal cord, we injected retrograde trans-multisynaptic pseudorabies virus (PRV) into the sciatic nerves of the rats. PRV$^+$ neurons and nerve fibers were

observed in the rostral region to the injury/graft site (Fig. 6a, a1 and b), and the injury/graft site (Fig. 6a, a2, a3 and c). IEM showed that PRV^+ nerve fibers formed a synapse-like structure with a GFP^+ neuron cell body (Fig. 6d and d1). A PRV^+ neuronal process from a postsynaptic element was observed next to the presynaptic element of the infected GFP^+ neurons (Fig. 6d1). Therefore, GFP^+ neurons in the injury/graft site infected the descending nerve fibers (Fig. 6e). For rats with T10 spinal cord transection, whether PRV was delivered to the cervical spinal cord or the motor cortex depended on the capability of GFP^+ interneurons in the transplanted area to deliver PRV. A greater number of PRV^+ neurons were observed in the regions rostral and caudal to/in the injury/graft site in the E-SCLT group than in the SCLT group (Fig. 6f, and Supplementary Fig. 7a and b), revealing that the SCLT in the E-SCLT group had integrated better with the spinal neural circuitry than that in the SCLT group.

3.7. Assessment of innervation, energy metabolism and regenerative microenvironment in paralyzed hindlimb muscle

To further explore how TNES alleviated muscle atrophy after SCI, we analyzed the muscle innervation and oxidative capacity in the paralyzed hindlimbs. In terms of innervation, hindlimb gastrocnemius motor endplates in SCLT group had more co-expressed SYP and α-bungarotoxin (α-BT) than those in the E-SCI group, while the E-SCI group had more $SYP^+/\alpha\text{-}BT^+$ motor endplates than the SCI group (Fig. 7a1–a5). In fact, more $\alpha\text{-}BT^+$ motor endplates with SYP^+/NF^+ nerve fibers were observed in the E-SCLT group than those in the SCLT group (Fig. 7b and c), whereas they were most abundant in the Nor group (Fig. 7d, see below for statistical details).

Few $Pax7^+$ (a marker of skeletal muscle stem cell) cells were observed in the hindlimb tibialis anterior in the Nor group, but there were more in the SCI group (Fig. 7e). $Pax7^+$ cells were more

abundant in the hindlimb tibialis anterior in the E-SCI, SCLT, and E-SCLT groups than in the SCI and Nor groups (Fig. 7e, see below for statistical details).

To investigate the oxidative capacity of the muscle after SCI, changes in proteins related to muscle oxidative metabolism in gastrocnemius tissue were tested via western blot. Levels of mitochondrial respiratory chain complex proteins (CV-ATP5A, CIII-UQCRC2, CIV-MTCO1, CII-SDHB and CI-NDUFB8) were highest in the E-SCLT group, followed by the SCLT and E-SCI groups (compared to the SCI group) (Fig. 7f and g). Mitochondrial respiratory chain complex protein levels in the E-SCLT and Nor groups were not significantly different (Fig. 7f and g), suggesting that oxidative metabolism in the gastrocnemius in the E-SCLT group returned to normal. Consistent with increased oxidative metabolism, SYP^+/α-BT^+ and $Pax7^+$ cells were most abundant in the E-SCLT group, followed by the SCLT and E-SCI groups (Fig. 7h and i), indicating increased muscle innervation and regeneration in the E-SCLT group. Changes in myosin heavy chain I (MHCI), growth differentiation factor 8 (GDF8, a myostatin), NT-3 (a neurotrophic factor), and insulin-like growth factor-1 (IGF-1, a myotrophic factor) proteins in gastrocnemius tissue were examined with western blotting. The levels of GDF8 were the highest in the SCI group, whereas MHCI was the lowest (Supplementary Fig. 8). The levels of GDF8 in the E-SCI, SCLT, and E-SCLT groups were lower by varying degrees compared to the SCI group; GDF8 levels were the lowest in the Nor group. In contrast, the levels of MHCI were higher by varying degrees in the E-SCI, SCLT, and E-SCLT groups than in the SCI group; MHCI was the highest in the Nor group (Supplementary Fig. 8).

Among the proteins associated with muscle growth, the levels of NT-3 and IGF-1 were the lowest in the SCI group. The levels of NT-3 and IGF-1 were higher by varying degrees in the E-SCI, SCLT, and E-SCLT groups and highest in the Nor group (Supplementary Fig. 8).

Furthermore, the transverse area of muscle fibers in the tibialis anterior in the SCI group was the smallest (Fig. 7j and Supplementary Fig. 9). The tibialis anterior in rats treated with TNES or with SCLT implants had higher (to varying degrees) areas of muscle fibers than that in rats in the SCI group. The area of muscle fibers in the E-SCLT group was the largest among all groups except the Nor group (Fig. 7j and Supplementary Fig. 9).

3.8. Retrograde neural pathway tracing and analysis of neuronal connections in injured spinal cord

To determine the influence of TNES on neurons in the lower thoracolumbar spinal cord that control hindlimb behavior and the donor neurons in the injury/graft site transmitting neural information, we injected FG into the sciatic nerve and PRV into the tail nerve. $EPHA4^+/VGluT2^+$ central pattern generator (CPG) [26] neurons in lower thorax spinal cord closely contacted migrating GFP^+ donor neurons from the injury/graft site in the E-SCLT group (Fig. 8a). These neurons were labeled with PRV (Fig. 8a1), indicating that PRV^+ CPG neurons retrogradely transferred PRV to transplanted neurons. As shown in Fig. 8b and c, $EPHA4^+/VGluT2^+$ neurons labeled with PRV derived from the rat tail showed PRV/EPHA4/VGluT2 staining at the L2 segment (Fig. 8c), revealing that the lumbosacral spinal anterior horn motor neurons dominating tail muscle activity form relevant neural circuit connections with CPG neurons. At the L4 segment, some motor neurons were co-labeled with FG and PRV derived from the hindlimbs and tail, respectively (Fig. 8d and d1, arrow), whereas others were labeled only with FG (Fig. 8d and d2, arrowhead). Subsequently, 3D reconstruction showed polypolar neurons with long processes labeled with FG or co-labeled with FG and PRV connected via their processes to form a neural network-like structure at the L4 segment (Supplementary Video 4). Thus, motor neurons in the

lumbar spinal cord mainly control hindlimb muscle activity and are associated with the tail muscle activity.

To identify an afferent pathway that receives electrical stimulation from the tail nerve, the non-transsynaptic cholera toxin B (CTB) was injected into the rat tail. Some CTB^+ nerve fibers were observed in the dorsal horn at the L2 segment (Fig. 8e) and formed contacts with $EPHA4^+/VGluT2^+$ neurons (Fig. 8e1 and e2), suggesting that electrical stimulation information received by the tail nerve can be transmitted to spinal cord CPG neurons through a relevant afferent pathway.

These results are summarized in a schematic diagram showing that PRV was injected into the rat tail muscle, retrogradely labeled lumbosacral spinal anterior horn motor neurons, and retrogradely transferred to interneurons (Fig. 8f). Another marker (FG) was injected into the sciatic nerve and retrogradely labeled motor neurons in the lumbar spinal cord anterior horn. PRV^+ interneurons also transferred PRV to FG^+ motor neurons through mutual synaptic structures, appearing as FG^+/PRV^+ motor neurons (Fig. 8f). A third marker (CTB) was injected into the tail to label afferent nerve fibers of dorsal root ganglion (DRG) sensory neurons, showing that afferent nerve fibers contact CPG neurons in injured spinal cord. Fig. 8g shows a schematic diagram of the electrical stimulation information that TNES transmits to the spinal cord neural network through the sensory afferent nerve in the tail. Neural information activates lumbar anterior horn motor neurons to prevent the atrophy of paralyzed hindlimb muscles and improve voluntary motor function.

4. Discussion

The latest strategies for SCI treatment focus primarily on the application of biological therapies, such as stem cell transplantation, to promote nerve regeneration at the injury site and

reconstruct neural circuits [5, 17, 27]. Potential questions associated with this approach include whether the correct synaptic connections between transplanted and spinal cord neurons can be established in a timely manner and how the functionally silent neural circuits below the injury site will be activated [5, 6, 28, 29]. Recent studies have suggested that the combined application of biological therapy and electrical nerve stimulation has important research and clinical value for activating the silent neural circuit and repairing voluntary motor function after SCI [21, 29-31]. In this study, SCLT transplantation was combined with TNES to treat complete spinal cord transection and explore a novel mechanism through which the combination synergizes in the repair of voluntary motor function after SCI.

The advantage of SCLT is that it directionally provides (both NSC-derived) oligodendrocytes to the spinal cord white matter and neurons to the gray matter through pre-induction of NSC differentiation *in vitro*. The neuronal processes grew to the white matter-like region and were surrounded by the myelin sheath formed by oligodendrocytes. Typical synapse-like connections were found between these neurons, which generated mEPSCs or mIPSCs. Thus, in the 3D collagen scaffold and associated 4D culture with the added time dimension, NSC-derived cells in the SCLT differentiated further, matured, and formed a microenvironment that was rich in neurotrophic factors and a unity of structure and function through close cell-cell interaction. Therefore, SCLT transplantation is more adaptable than direct-cell transplantation to the injury site and realizes better functional integration with the spinal cord [7, 27].

Our previous results suggested that SCLT transplanted into an SCI survives well, promotes nerve regeneration and myelin formation, and forms synapse-like connections with regenerated nerve fibers. However, two months after SCI the hindlimb muscles of rats with complete spinal cord transection normally exhibit an irreversible atrophy [7, 12]. Previous researchers

hypothesized that prior to the functional integration of SCLT with regenerated nerve fibers, functional silencing, excitatory inhibition, and neuromuscular degeneration all occur in the neural circuit below injury/graft site [2, 10]. More recently, researchers reported that the application of programmed precise EES of neural circuits with functional silence below the injury could restore muscle control and walking ability [32]. In another study, rats with SCI treated with TNES experienced a significant improvement in hindlimb muscle atrophy [12]. We hypothesized that the combination of SCLT with electrical stimulation could activate neural circuits and represents an important concept for spinal cord repair.

It has recently been reported that after SCI in adult mice, excitatory interneurons in the motor neural circuit below the injury site can be transformed into inhibitory phenotypes, thus resulting in the inhibition of synapses innervating the motor neurons; this leads to functional silencing of the motor neural circuit [33]. Excitatory interneurons are commonly thought to represent the sub-set of neurons that connect motor and sensory neurons in the spinal cord and take advantage of the neurotransmitter glutamic acid to transmit signals. Moreover, spinal motor neurons are the final units that regulate limb movement. Therefore, nerve electrical stimulation can be applied to convert interneurons below the injury site into excitatory phenotypes to activate the motor neural circuit that has been functionally silenced, thus improving motor function in the paralyzed limbs [34]. In the present study, we observed further improvement in voluntary motor functionality, as evidenced by the achievement of coordinated forelimb and hindlimb movement and weight-bearing walking in rats that underwent SCLT transplantation combined with TNES. CMEPs indicated that neural signals from the brain were robustly transmitted to neurons that dominate hindlimb movement because of the synergistic effect between SCLT transplantation and TNES.

Nerve fiber regeneration and myelin sheath formation in the region caudal to/in the injury/graft site were higher in the E-SCLT group than in other groups, suggesting that TNES promotes the integration of SCLT with the caudal spinal cord. A higher proportion of NSC-derived donor neurons in the injury/graft site after TNES were excitatory, indicating that the phenotype changed. These findings suggested that TNES enhanced the integration of SCLT with the caudal spinal cord through regulating neural plasticity, such that the SCLT relayed more excitatory neural signals to the caudal spinal neural circuit. Level of cytoskeleton-associated protein Arc was significantly higher in the caudal spinal cord below the injury/graft site in rats treated with TNES, confirming that electrical stimulation causes excitability and synaptic plasticity of the caudal spinal neural circuit [35]. Detection of c-Fos indicated that TNES retrogradely activated $VGluT1^+$ neurons in L1 dorsal nucleus and NSC-derived donor neurons, further confirming the existence of a neural pathway via which TNES promotes synaptic plasticity and the functional integration of transplanted neurons with caudal spinal neural circuits [36]. We detected higher levels of synapse-related proteins PSD95 and SYP and the motor neuron-related neurotransmitter synthase ChAT in the caudal spinal cord of rats transplanted with SCLT and treated by TNES, suggesting the importance of TNES in activating spinal motor neural circuits and regulating neural plasticity [4, 35]. NT-3 levels in the caudal spinal cord were higher in rats transplanted with SCLT treated with TNES (Fig. 4i and j). The possible mechanism is that TNES acts on tail afferent nerve fibers derived from calcitonin gene-related peptide (CGRP)-positive sensory neurons, and increases the release of CGRP into the spinal cord via their nerve endings [37-39]. CGRP acts on spinal cord neurons expressing receptor activity-modifying protein (RAMP), and stimulates the opening of L-type voltage-gated Ca^{2+} channels (L-VGCC) on the cell membrane and Ca^{2+} influx; this process activates calcium/calmodulin-dependent protein kinase (αCaMKII) signaling and the expression

of NT-3 [37]. We speculate that TrkC-overexpressing donor neuronal axons are induced to innervate activated neurons in caudal spinal cord upon the release of NT-3 (Supplementary Fig. 5 and Supplementary Fig. 6). The synergistic effect of TNES is similar to a mechanism we previously reported that electro-acupuncture stimulation could improve the microenvironment of transected SCI to promote the reconstruction of neural circuits between transplanted neurons and lumbar spinal cord neurons [31, 37, 40]. These data indicate that TNES improved the microenvironment to promote the functional integration of transplanted neurons with the caudal spinal neural circuit.

TNES promotes the integration of SCLT with the neural circuit of the injured spinal cord, which is supported by the larger number of regenerating VGluT1$^+$ nerve fibers found in the regions rostral and caudal to/in the injury/graft side after electrical stimulation. Functional integration may contribute to the relay of brain-derived excitatory neural signals [5, 16]. IEM indicated that VGluT1$^+$ nerve fibers formed synapse-like connections with NSC-derived donor neurons in the injury/graft site. PRV-labeled neurons were found in the regions rostral and caudal to/in the injury/graft site following the PRV sciatic nerve injection, especially in the EPHA4$^+$/VGluT2$^+$ neurons in the lumbar spinal cord, in the thoracic spinal cord and pyramidal cells in the cerebral motor cortex. These data further support the assumption that TNES efficiently promotes the establishment of functional synaptic connections between SCLT and brain-derived descending nerve fibers that relay excitatory neural signals to EPHA4$^+$/VGluT2$^+$ CPG neurons in the lumbar spinal cord to activate those controlling movement in the hindlimbs. Recently, Kathe et al. reported the use of a mouse model of T8 SCI to determine that excitatory interneurons of the Vsx2$^+$ in the lumbar spinal cord play an important role in the reconstruction of motor function in the hindlimbs after EES [1]. In our study, we discovered the importance of EPHA4$^+$/VGluT2$^+$ neurons in the

lumbar spinal cord in TNES treatment. We hypothesize that after the loss of brain-derived neural afferents in the lumbar spinal cord, the regulation of these two subtypes of neurons by nerve electrical stimulation may play an important synergistic role in remodeling of the motor neural network.

TNES further strengthens the efficiency of SCLT in relaying brain-derived neural signals. SCLT transplantation and TNES synergized in the innervation of motor endplates and activation of $Pax7^+$ muscle stem cells in paralyzed hindlimb skeletal muscles. $Pax7^+$ muscle stem cells can not only differentiate into new muscle fibers during muscle tissue regeneration, but also fuse with and enhance protein synthesis and energy metabolism the original muscle fibers, which is of great significance for muscle regeneration and recovery of muscle function [41, 42]. TNES improved the muscle regenerative microenvironment and promoted mitochondrial energy. These results demonstrate a mechanism by which the combination of SCLT transplantation with TNES prevents muscle atrophy and improves hindlimb motor function after SCI.

To further investigate the potential neural pathway responsible for the effects of TNES, we used retrograde dual nerve tracers. PRV injected into rat tails retrogradely infected L5 and L4 spinal cord motor neurons, those innervating hindlimb muscles, and CPG neurons of the L1 and L2 spinal cord through synaptic connections. Tail nerve tracing suggested that transplanted neurons in the SCLT formed synaptic connections with CPG neurons in the lower thoracolumbar spinal cord, facilitating the reception of brain-derived neural information relayed by transplanted neurons by $EPHA4^+/VGluT2^+$ CPG neurons. Therefore, the neuromodulatory effect of TNES improves the innervation between the brain, motor neurons in lumbar spinal cord, and hindlimb muscles after SCLT transplantation. Similarly, CTB tracing in the tail nerve revealed that TNES affects CPG neurons and motor neural circuits through sensory afferent fibers [26]. These neural

circuits are the structural basis for enhanced energy metabolism, reduced muscle atrophy, and restored hindlimb supported weight standing and walking promoted by TNES-activated motor neurons.

The results are summarized in the schematic diagram showing that PRV injected into the rat tail retrogradely labeled lumbosacral spinal cord anterior horn motor neurons and subsequently retrogradely transferred to interneurons (Fig. 8f). Another tracer, FG, was injected into the sciatic nerve and retrogradely labeled motor neurons in the lumbar spinal cord anterior horn. PRV^+ interneurons also transferred PRV to FG^+ motor neurons through mutual synapse-like structures, appearing as PRV^+/FG^+ motor neurons (Fig. 8f). A third tracer (CTB) injected into the tail labeled afferent nerve fibers of DRG sensory neurons, showing that afferent nerve fibers contacted CPG neurons in injured spinal cord. CPG neurons may secrete NT-3 to guide the TrkC-overexpressing axons derived from the donor neurons in the injury/graft site to innervate them (Fig. 8f). The electrical information provided by TNES is transmitted to the spinal cord neural network through the tail sensory afferent nerve (Fig. 8g). Electrical stimulation promotes the integration of SCLT and the regenerated nerve fibers and the SCLT relay of brain-derived neural signals to the caudal spinal cord. TNES also activates motor neurons in lumbar anterior horn to prevent the atrophy of paralyzed hindlimb muscles and improve voluntary motor function.

5. Conclusion

The use of retrograde dual nerve tracers in the tail and sciatic nerves revealed the mechanism by which TNES activated the caudal spinal cord motor neural circuit and promoted the integration of SCLT with the spinal cord, realizing the recovery of voluntary motor function through neuromodulation. Therefore, TNES played a significant role in synergistic electrical stimulation

and may promote the dynamic integration and functional coordination of transplanted neurons at the injury site with the ascending and descending axons. This process involves repeated synaptic activation which enhances synaptic plasticity in the neural circuits between glutaminergic interneurons and motor neurons [33], and thus reconstitutes the spinal cord neural network and promotes the effective transmission of brain-derived excitatory information, and eventually improves the motor function. Although both nerve electrical stimulation and rehabilitation are greatly helpful in functional improvements, some studies have shown that performing nerve electrical stimulation alone without rehabilitation can also improve motor function [4, 43, 44]. This finding is important because many SCI patients have severe injuries which hinder them from receiving rehabilitation [45]. In conclusion, the combined therapeutic strategy of neuronal relay and activation of the functionally silent caudal spinal cord has greater advantages in application and prospects over current clinical treatments to achieve better recovery of voluntary motor function in the future clinical treatment of SCI [4, 30, 46]. Future research into multimodal regimens for complex SCI should investigate whether more accurate electrical stimulation to promote better functional integration between transplanted neurons and the injured spinal cord improves voluntary motor function in a more robust manner.

Author contributions

YSZ, QJZ, and YFC designed and supervised the study. BQL, RJW, WTH, YRB, JLL, HYY, SBY, LJW, JLR, and YQW performed the experiments and collected the data. BQL, RJW, WTH, and YSZ summarized, analyzed, and plotted the data and drafted the manuscript. YD, GL, XZ, YHM, QQ, LYX, BJ, LZ, and ZHC helped with study planning and critically reviewed the manuscript. BQL, YSZ and RJW wrote and finalized the article.

Declaration of competing interest

The authors declare that they have no known competing financial interests or personal relationships that could have appeared to influence the work reported in this paper.

Acknowledgements

This research was supported by grants from the National Natural Science Foundation of China (Grant No. 81891003 to Y.S. Zeng and 81971157 to B.Q. Lai), the National Key R&D Program of China (No.2022YFA1105900 and No.2017YF010A4704 to B.Q. Lai) and the Natural Science Foundation of Guangdong Province, China (No. 2021B1515020045 to B.Q. Lai).

Appendix A. Supplementary data

Supplementary data to this article can be found online at https://doi. org/10.1016/j.biomaterials.

REFERENCES

[1] C. Kathe, M.A. Skinnider, T.H. Hutson, N. Regazzi, M. Gautier, R. Demesmaeker, S. Komi, S. Ceto, N.D. James, N. Cho, L. Baud, K. Galan, K.J.E. Matson, A. Rowald, K. Kim, R. Wang, K. Minassian, J.O. Prior, L. Asboth, Q. Barraud, S.P. Lacour, A.J. Levine, F. Wagner, J. Bloch, J.W. Squair, G. Courtine, The neurons that restore walking after paralysis, Nature 611(7936) (2022) 540-547.

[2] M.L. Gill, P.J. Grahn, J.S. Calvert, M.B. Linde, I.A. Lavrov, J.A. Strommen, L.A. Beck, D.G. Sayenko, M.G. Van Straaten, D.I. Drubach, D.D. Veith, A.R. Thoreson, C. Lopez, Y.P.

Gerasimenko, V.R. Edgerton, K.H. Lee, K.D. Zhao, Neuromodulation of lumbosacral spinal networks enables independent stepping after complete paraplegia, Nature medicine 24(11) (2018) 1677-1682.

[3] V. Van Steenbergen, L. Burattini, M. Trumpp, J. Fourneau, A. Aljović, M. Chahin, H. Oh, M. D'Ambra, F.M. Bareyre, Coordinated neurostimulation promotes circuit rewiring and unlocks recovery after spinal cord injury, The Journal of experimental medicine 220(3) (2023).

[4] D. Silva, L. Schirmer, T.S. Pinho, P. Atallah, J.R. Cibrão, R. Lima, J. Afonso, B.A. S, C.R. Marques, J. Dourado, U. Freudenberg, R.A. Sousa, C. Werner, A.J. Salgado, Sustained Release of Human Adipose Tissue Stem Cell Secretome from Star-Shaped Poly(ethylene glycol) Glycosaminoglycan Hydrogels Promotes Motor Improvements after Complete Transection in Spinal Cord Injury Rat Model, Advanced healthcare materials (2023) e2202803.

[5] S. Ceto, K.J. Sekiguchi, Y. Takashima, A. Nimmerjahn, M.H. Tuszynski, Neural Stem Cell Grafts Form Extensive Synaptic Networks that Integrate with Host Circuits after Spinal Cord Injury, Cell stem cell 27(3) (2020) 430-440.e5.

[6] N.S. Lavoie, V. Truong, D. Malone, T. Pengo, N. Patil, J.R. Dutton, A.M. Parr, Human induced pluripotent stem cells integrate, create synapses and extend long axons after spinal cord injury, Journal of cellular and molecular medicine (2022).

[7] B.Q. Lai, B. Feng, M.T. Che, L.J. Wang, S. Cai, M.Y. Huang, H.Y. Gu, B. Jiang, E.A. Ling, M. Li, X. Zeng, Y.S. Zeng, A Modular Assembly of Spinal Cord-Like Tissue Allows Targeted Tissue Repair in the Transected Spinal Cord, Advanced science (Weinheim, Baden-Wurttemberg, Germany) 5(9) (2018) 1800261.

[8] W. Wu, S. Jia, H. Xu, Z. Gao, Z. Wang, B. Lu, Y. Ai, Y. Liu, R. Liu, T. Yang, R. Luo, C. Hu, L. Kong, D. Huang, L. Yan, Z. Yang, L. Zhu, D. Hao, Supramolecular Hydrogel Microspheres of Platelet-Derived Growth Factor Mimetic Peptide Promote Recovery from Spinal Cord Injury, ACS nano 17(4) (2023) 3818-3837.

[9] Q. Han, J.D. Ordaz, N.K. Liu, Z. Richardson, W. Wu, Y. Xia, W. Qu, Y. Wang, H. Dai, Y.P. Zhang, C.B. Shields, G.M. Smith, X.M. Xu, Descending motor circuitry required for NT-3 mediated locomotor recovery after spinal cord injury in mice, Nature communications 10(1) (2019) 5815.

[10] B. Chen, Y. Li, B. Yu, Z. Zhang, B. Brommer, P.R. Williams, Y. Liu, S.V. Hegarty, S. Zhou, J. Zhu, H. Guo, Y. Lu, Y. Zhang, X. Gu, Z. He, Reactivation of Dormant Relay Pathways in Injured Spinal Cord by KCC2 Manipulations, Cell 174(3) (2018) 521-535 e13.
[11] S.O.M. Fideles, A. de Cássia Ortiz, D.V. Buchaim, E. de Souza Bastos Mazuqueli Pereira, M. Parreira, J. de Oliveira Rossi, M.R. da Cunha, A.T. de Souza, W.C. Soares, R.L. Buchaim, Influence of the Neuroprotective Properties of Quercetin on Regeneration and Functional Recovery of the Nervous System, Antioxidants (Basel, Switzerland) 12(1) (2023).
[12] Y.T. Zhang, H. Jin, J.H. Wang, L.Y. Wen, Y. Yang, J.W. Ruan, S.X. Zhang, E.A. Ling, Y. Ding, Y.S. Zeng, Tail Nerve Electrical Stimulation and Electro-Acupuncture Can Protect Spinal Motor Neurons and Alleviate Muscle Atrophy after Spinal Cord Transection in Rats, Neural plasticity 2017 (2017) 7351238.
[13] Y. Huang, J. Wang, C. Yue, R. Wang, Q. Guo, T. Wang, D. Wang, H. Dong, Y. Hu, G. Tao, X. Li, An In Situ Assembled Trapping Gel Repairs Spinal Cord Injury by Capturing Glutamate and Free Calcium Ions, Small (Weinheim an der Bergstrasse, Germany) (2023) e2206229.
[14] H. Liu, X. Xu, Y. Tu, K. Chen, L. Song, J. Zhai, S. Chen, L. Rong, L. Zhou, W. Wu, K.F. So, S. Ramakrishna, L. He, Engineering Microenvironment for Endogenous Neural Regeneration after Spinal Cord Injury by Reassembling Extracellular Matrix, ACS applied materials & interfaces 12(15) (2020) 17207-17219.
[15] R.E. Thompson, J. Pardieck, L. Smith, P. Kenny, L. Crawford, M. Shoichet, S. Sakiyama-Elbert, Effect of hyaluronic acid hydrogels containing astrocyte-derived extracellular matrix and/or V2a interneurons on histologic outcomes following spinal cord injury, Biomaterials 162 (2018) 208-223.
[16] B.Q. Lai, M.T. Che, B. Feng, Y.R. Bai, G. Li, Y.H. Ma, L.J. Wang, M.Y. Huang, Y.Q. Wang, B. Jiang, Y. Ding, X. Zeng, Y.S. Zeng, Tissue-Engineered Neural Network Graft Relays Excitatory Signal in the Completely Transected Canine Spinal Cord, Advanced science (Weinheim, Baden-Wurttemberg, Germany) 6(22) (2019) 1901240.
[17] L. Wertheim, R. Edri, Y. Goldshmit, T. Kagan, N. Noor, A. Ruban, A. Shapira, I. Gat-Viks, Y. Assaf, T. Dvir, Regenerating the Injured Spinal Cord at the Chronic Phase by Engineered iPSCs-Derived 3D Neuronal Networks, Advanced science (Weinheim, Baden-Wurttemberg, Germany) 9(11) (2022) e2105694.

[18] Y. Zou, Y. Yin, Z. Xiao, Y. Zhao, J. Han, B. Chen, B. Xu, Y. Cui, X. Ma, J. Dai, Transplantation of collagen sponge-based three-dimensional neural stem cells cultured in a RCCS facilitates locomotor functional recovery in spinal cord injury animals, Biomaterials science 10(4) (2022) 915-924.
[19] A. Zarepour, S. Hooshmand, A. Gökmen, A. Zarrabi, E. Mostafavi, Spinal Cord Injury Management through the Combination of Stem Cells and Implantable 3D Bioprinted Platforms, Cells 10(11) (2021).
[20] I. Woods, C. O'Connor, L. Frugoli, S. Kerr, J. Gutierrez Gonzalez, M. Stasiewicz, T. McGuire, B. Cavanagh, A. Hibbitts, A. Dervan, F.J. O'Brien, Biomimetic Scaffolds for Spinal Cord Applications Exhibit Stiffness-Dependent Immunomodulatory and Neurotrophic Characteristics, Advanced healthcare materials 11(3) (2022) e2101663.
[21] D. Becker, D.S. Gary, E.S. Rosenzweig, W.M. Grill, J.W. McDonald, Functional electrical stimulation helps replenish progenitor cells in the injured spinal cord of adult rats, Experimental neurology 222(2) (2010) 211-8.
[22] S. Chandrasekaran, J. Davis, I. Bersch, G. Goldberg, A.S. Gorgey, Electrical stimulation and denervated muscles after spinal cord injury, Neural regeneration research 15(8) (2020) 1397-1407.
[23] C.D. Dürst, J.S. Wiegert, N. Helassa, S. Kerruth, C. Coates, C. Schulze, M.A. Geeves, K. Török, T.G. Oertner, High-speed imaging of glutamate release with genetically encoded sensors, Nature protocols 14(5) (2019) 1401-1424.
[24] D.M. Basso, M.S. Beattie, J.C. Bresnahan, A sensitive and reliable locomotor rating scale for open field testing in rats, Journal of neurotrauma 12(1) (1995) 1-21.
[25] A. Pajoohesh-Ganji, K.R. Byrnes, G. Fatemi, A.I. Faden, A combined scoring method to assess behavioral recovery after mouse spinal cord injury, Neuroscience research 67(2) (2010) 117-25.
[26] K. Kullander, S.J. Butt, J.M. Lebret, L. Lundfald, C.E. Restrepo, A. Rydstrom, R. Klein, O. Kiehn, Role of EphA4 and EphrinB3 in local neuronal circuits that control walking, Science (New York, N.Y.) 299(5614) (2003) 1889-92.
[27] C.M. Zipser, J.J. Cragg, J.D. Guest, M.G. Fehlings, C.R. Jutzeler, A.J. Anderson, A. Curt, Cell-based and stem-cell-based treatments for spinal cord injury: evidence from clinical trials, The Lancet. Neurology 21(7) (2022) 659-670.

[28] K.A. Han, D. Woo, S. Kim, G. Choii, S. Jeon, S.Y. Won, H.M. Kim, W.D. Heo, J.W. Um, J. Ko, Neurotrophin-3 Regulates Synapse Development by Modulating TrkC-PTPsigma Synaptic Adhesion and Intracellular Signaling Pathways, The Journal of neuroscience : the official journal of the Society for Neuroscience 36(17) (2016) 4816-31.
[29] N.D. James, S.B. McMahon, E.C. Field-Fote, E.J. Bradbury, Neuromodulation in the restoration of function after spinal cord injury, The Lancet. Neurology 17(10) (2018) 905-917.
[30] A.L. O'Brein, J.M. West, T.M. Saffari, M. Nguyen, A.M. Moore, Promoting Nerve Regeneration: Electrical stimulation, stem cells and beyond, Physiology (Bethesda, Md.) (2022).
[31] H. Jin, Y.T. Zhang, Y. Yang, L.Y. Wen, J.H. Wang, H.Y. Xu, B.Q. Lai, B. Feng, M.T. Che, X.C. Qiu, Z.L. Li, L.J. Wang, J.W. Ruan, B. Jiang, X. Zeng, Q.W. Deng, G. Li, Y. Ding, Y.S. Zeng, Electroacupuncture Facilitates the Integration of Neural Stem Cell-Derived Neural Network with Transected Rat Spinal Cord, Stem cell reports 12(2) (2019) 274-289.
[32] A. Rowald, S. Komi, R. Demesmaeker, E. Baaklini, S.D. Hernandez-Charpak, E. Paoles, H. Montanaro, A. Cassara, F. Becce, B. Lloyd, T. Newton, J. Ravier, N. Kinany, M. D'Ercole, A. Paley, N. Hankov, C. Varescon, L. McCracken, M. Vat, M. Caban, A. Watrin, C. Jacquet, L. Bole-Feysot, C. Harte, H. Lorach, A. Galvez, M. Tschopp, N. Herrmann, M. Wacker, L. Geernaert, I. Fodor, V. Radevich, K. Van Den Keybus, G. Eberle, E. Pralong, M. Roulet, J.B. Ledoux, E. Fornari, S. Mandija, L. Mattera, R. Martuzzi, B. Nazarian, S. Benkler, S. Callegari, N. Greiner, B. Fuhrer, M. Froeling, N. Buse, T. Denison, R. Buschman, C. Wende, D. Ganty, J. Bakker, V. Delattre, H. Lambert, K. Minassian, C.A.T. van den Berg, A. Kavounoudias, S. Micera, D. Van De Ville, Q. Barraud, E. Kurt, N. Kuster, E. Neufeld, M. Capogrosso, L. Asboth, F.B. Wagner, J. Bloch, G. Courtine, Activity-dependent spinal cord neuromodulation rapidly restores trunk and leg motor functions after complete paralysis, Nature medicine 28(2) (2022) 260-271.
[33] H. Bertels, G. Vicente-Ortiz, K. El Kanbi, A. Takeoka, Neurotransmitter phenotype switching by spinal excitatory interneurons regulates locomotor recovery after spinal cord injury, Nature neuroscience 25(5) (2022) 617-629.
[34] K.W. Huang, E. Azim, Neurons that promote recovery from paralysis identified, Nature 611(7936) (2022) 452-453.

[35] A.W. Kraft, A.Q. Bauer, J.P. Culver, J.M. Lee, Sensory deprivation after focal ischemia in mice accelerates brain remapping and improves functional recovery through Arc-dependent synaptic plasticity, Science translational medicine 10(426) (2018).
[36] I.J. Llewellyn-Smith, C.L. Martin, N.M. Fenwick, S.E. Dicarlo, H.L. Lujan, A.M. Schreihofer, VGLUT1 and VGLUT2 innervation in autonomic regions of intact and transected rat spinal cord, The Journal of comparative neurology 503(6) (2007) 741-67.
[37] Y.S. Zeng, Y. Ding, H.Y. Xu, X. Zeng, B.Q. Lai, G. Li, Y.H. Ma, Electro-acupuncture and its combination with adult stem cell transplantation for spinal cord injury treatment: A summary of current laboratory findings and a review of literature, CNS neuroscience & therapeutics 28(5) (2022) 635-647.
[38] J.C. Eisenach, Y. Zhang, F. Duflo, alpha2-adrenoceptors inhibit the intracellular Ca2+ response to electrical stimulation in normal and injured sensory neurons, with increased inhibition of calcitonin gene-related peptide expressing neurons after injury, Neuroscience 131(1) (2005) 189-97.
[39] H. Xu, Y. Yang, Q.W. Deng, B.B. Zhang, J.W. Ruan, H. Jin, J.H. Wang, J. Ren, B. Jiang, J.H. Sun, Y.S. Zeng, Y. Ding, Governor Vessel Electro-Acupuncture Promotes the Intrinsic Growth Ability of Spinal Neurons through Activating Calcitonin Gene-Related Peptide/α-Calcium/Calmodulin-Dependent Protein Kinase/Neurotrophin-3 Pathway after Spinal Cord Injury, Journal of neurotrauma 38(6) (2021) 734-745.
[40] Y. Yang, H.Y. Xu, Q.W. Deng, G.H. Wu, X. Zeng, H. Jin, L.J. Wang, B.Q. Lai, G. Li, Y.H. Ma, B. Jiang, J.W. Ruan, Y.Q. Wang, Y. Ding, Y.S. Zeng, Electroacupuncture facilitates the integration of a grafted TrkC-modified mesenchymal stem cell-derived neural network into transected spinal cord in rats via increasing neurotrophin-3, CNS neuroscience & therapeutics 27(7) (2021) 776-791.
[41] Y. Liang, H. Han, Q. Xiong, C. Yang, L. Wang, J. Ma, S. Lin, Y.Z. Jiang, METTL3-Mediated m(6)A Methylation Regulates Muscle Stem Cells and Muscle Regeneration by Notch Signaling Pathway, Stem cells international 2021 (2021) 9955691.
[42] Y.Y. Zheng, Y. Wang, X. Chen, L.S. Wei, H. Wang, T. Tao, Y.W. Zhou, Z.H. Jiang, T.T. Qiu, Z.Y. Sun, J. Sun, P. Wang, W. Zhao, Y.Q. Li, H.Q. Chen, M.S. Zhu, X.N. Zhang, The thymus regulates skeletal muscle regeneration by directly promoting satellite cell expansion, The Journal of biological chemistry 298(1) (2022) 101516.

[43] J.B. Carmel, L.J. Berrol, M. Brus-Ramer, J.H. Martin, Chronic electrical stimulation of the intact corticospinal system after unilateral injury restores skilled locomotor control and promotes spinal axon outgrowth, The Journal of neuroscience : the official journal of the Society for Neuroscience 30(32) (2010) 10918-26.
[44] N. Zareen, M. Shinozaki, D. Ryan, H. Alexander, A. Amer, D.Q. Truong, N. Khadka, A. Sarkar, S. Naeem, M. Bikson, J.H. Martin, Motor cortex and spinal cord neuromodulation promote corticospinal tract axonal outgrowth and motor recovery after cervical contusion spinal cord injury, Experimental neurology 297 (2017) 179-189.
[45] R. Steensgaard, R. Kolbaek, S. Angel, Nursing staff facilitate patient participation by championing the patient's perspective: An action research study in spinal cord injury rehabilitation, Health expectations : an international journal of public participation in health care and health policy 25(5) (2022) 2525-2533.
[46] B.Q. Lai, X. Zeng, W.T. Han, M.T. Che, Y. Ding, G. Li, Y.S. Zeng, Stem cell-derived neuronal relay strategies and functional electrical stimulation for treatment of spinal cord injury, Biomaterials 279 (2021) 121211.

Figures and Figure Legends：

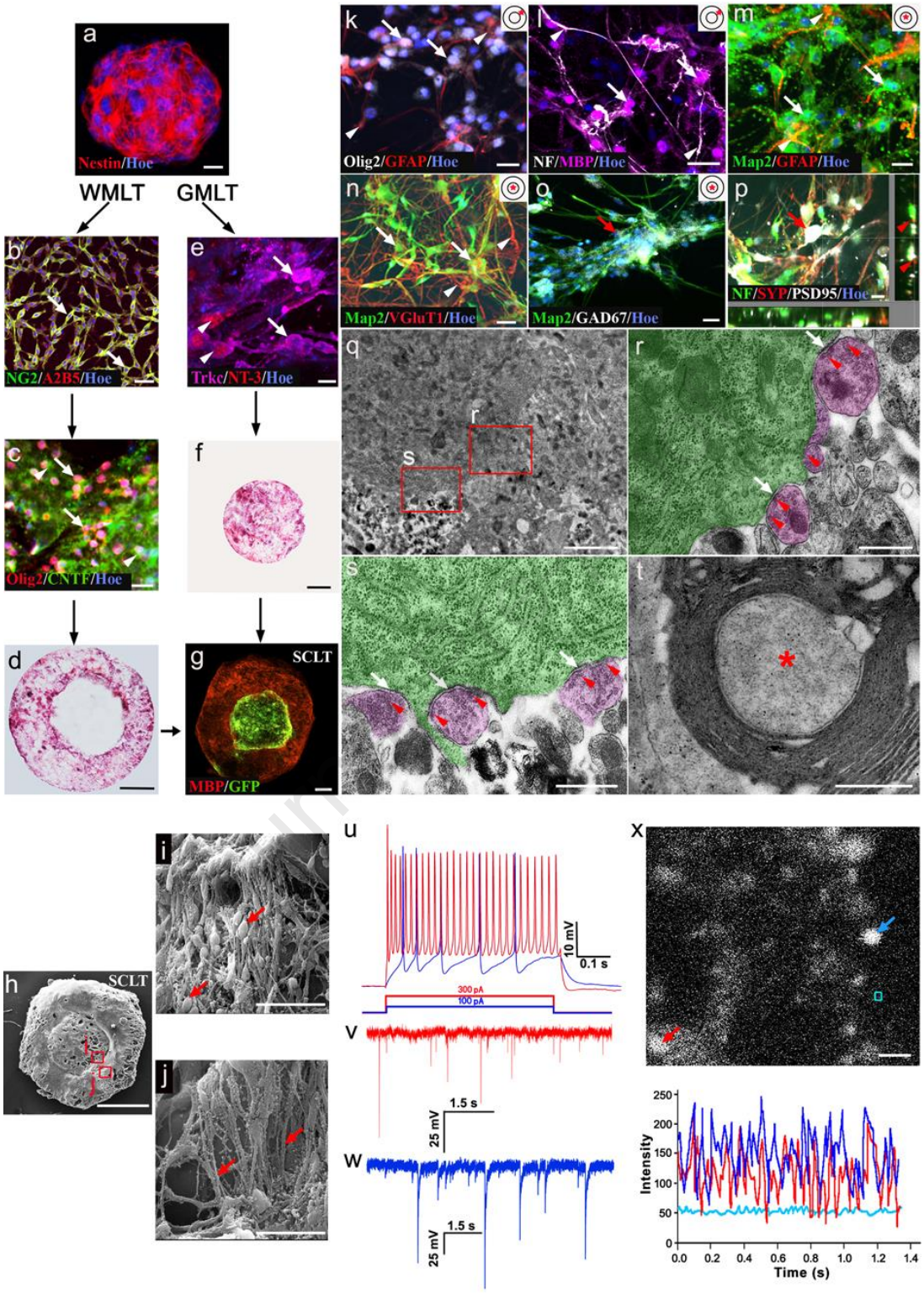

Fig. 1. Assembly of the SCLT simulating spinal cord. a-g) Construction of the SCLT. A neurosphere with Nestin^{+} cells (a). NG2^{+} and A2B5^{+} cells in OPCs (b, arrows). Olig2^{+} (arrows) and CNTF^{+} (arrowheads) cells in WMLT after transfection (c). H&E staining of the WMLT (d).

NT-3$^+$ (arrowheads) and TrkC$^+$ (arrows) cells in GMLT after transfection (e). H&E staining of the GMLT (f). Distinct partition of the WMLT module (MBP$^+$) and GMLT module (GFP$^+$) after being assembled into a SCLT for 7 days (g). h–j) SCLT visualized with SEM. k–p) Phenotype differentiation and surface marker of SCLT cells; q–t) Synapses and myelin sheaths in the SCLT visualized with TEM. u–w) Evoked action potentials and postsynaptic currents were recorded in the SCLT. x) Dynamic fluorescence changes in the glutamate sensor iGluSnFR after glutamate stimulation (arrow and box colors corresponds to the curve of fluorescence intensity change at the observation point). Scale bars = 20 μm in (a, c, d, k, m, o, p, x); 50 μm in (b, l); 500 μm in (e–g); 1 mm in (h); 40 μm in (i, j); 30 μm in (n); 2 μm in (q); 500 nm in (r, t); 200 nm in (s).

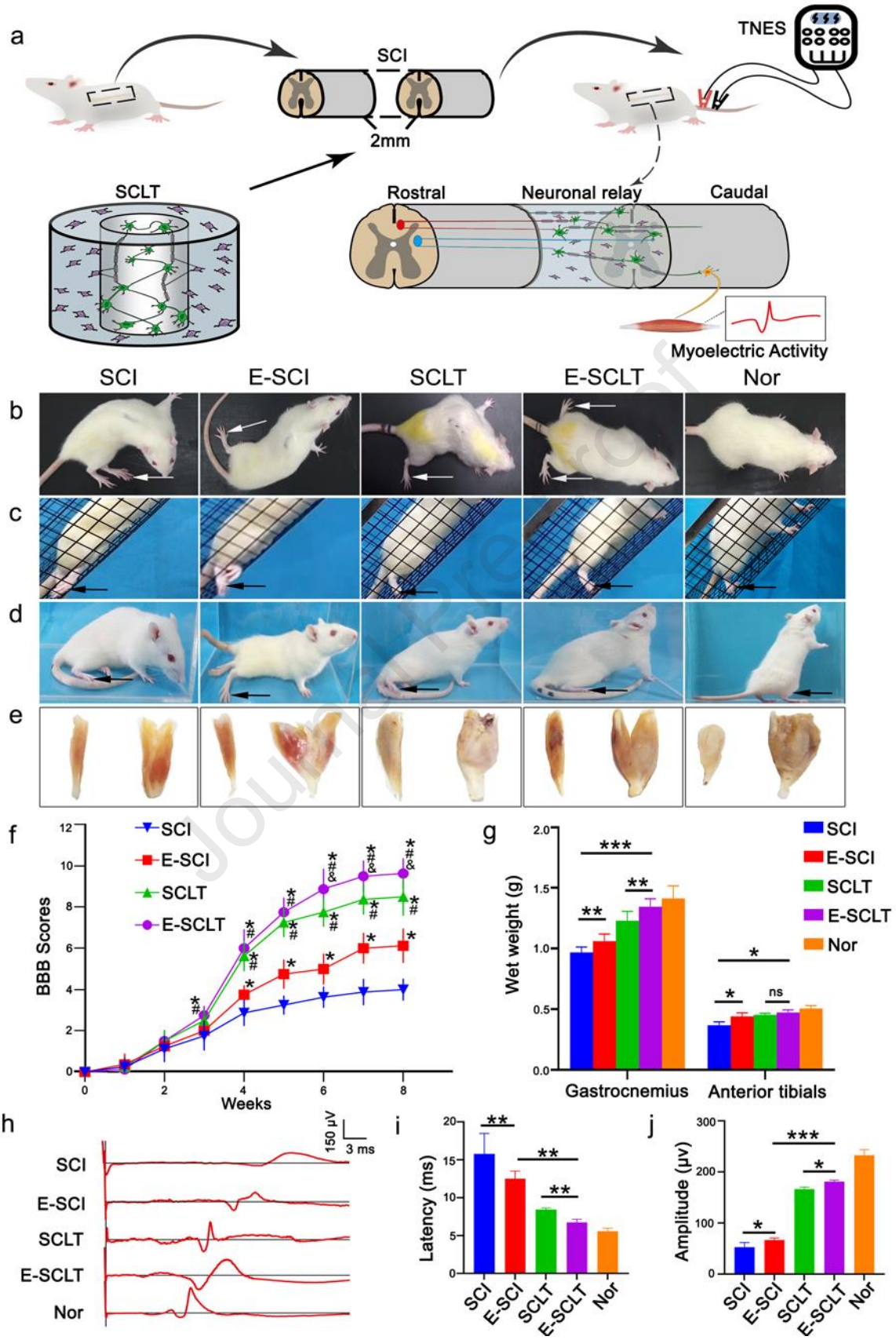

Fig. 2. Analyses of behavior, muscle wet weight, and electrophysiological outcomes. a) Schematic diagram of the combination of TNES and SCLT transplantation to treat SCI rats. b) Open-field observation. c) Inclined grid climbing test. d) Glass cube observation showed that rats receiving TNES and SCLT transplantation displayed the best supporting body weight behavior (except for the Nor group), followed by the E-SCI and SCLT groups. e) TNES alleviated gastrocnemius and the tibialis anterior atrophy. f) BBB scoring significantly increased in the hindlimb motor function following TNES treatment and SCLT transplant (*, $^{\#}$, and $^{\&}$ indicate statistical significance when compared with the SCI, E-SCI, and SCLT groups, respectively, $P < 0.05$). g) Gastrocnemius and tibialis anterior muscle wet weights (*$P < 0.05$, **$P < 0.01$). h) Rats in the E-SCLT group had higher CMEP amplitudes than those in the SCLT group, whereas there was no difference in latency. CMEP latencies and amplitudes were different between the SCI and the E-SCI groups (*$P < 0.05$, **$P < 0.01$).

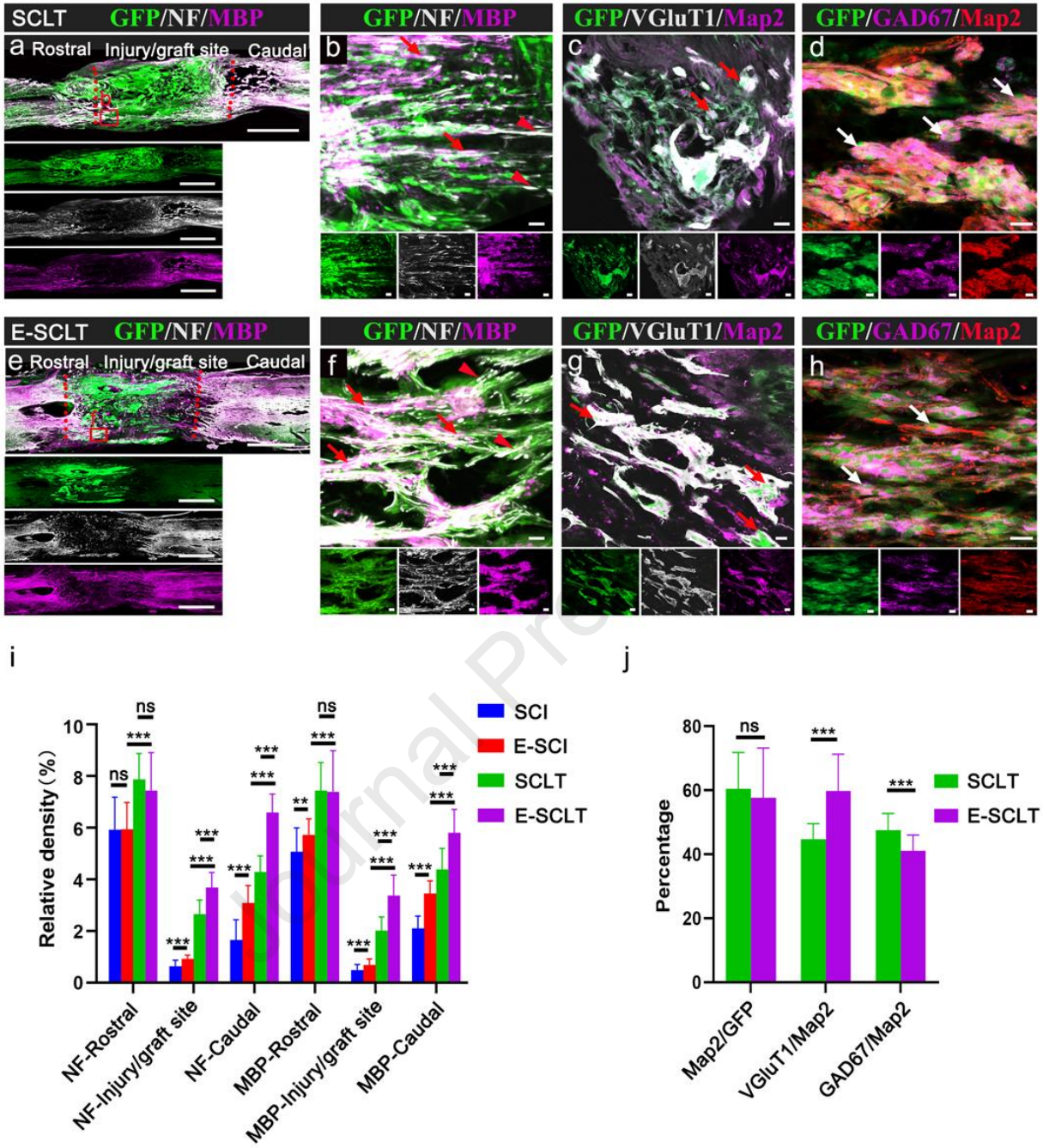

Fig. 3. Assessment of nerve fibers, myelination and differentiated neurons in the injury/graft site. a) Low magnification of sagittal spinal cord section showing the expression of NF and MBP in the SCLT group. b) GFP^+/NF^+ nerve fibers (arrowheads) wrapped with MBP^+ cells (arrows). c) $VGluT1^+$ neurons in the SCLT group (arrows). d) $GAD67^+$ neurons in the SCLT group (arrows). e) Low magnification of sagittal spinal cord section showing the expression of NF and MBP in the E-SCLT group. f) More GFP^+/NF^+ nerve fibers (arrowheads) were wrapped with

MBP$^+$ cells (arrows) in the E-SCLT group than those in the SCLT group. g) More VGluT1$^+$ neurons were found in the E-SCLT group than those in the SCLT group (arrows). h) Fewer GAD67$^+$ neurons were found in the E-SCLT group than those in the SCLT group (arrows). i) Relative density of NF and MBP in the SCLT and E-SCLT groups. j) Percentages of Map2$^+$ neurons among all GFP$^+$ cells and of VGluT1$^+$ and GAD67$^+$ cells among all Map2$^+$ cells. $*P < 0.05$, $**P < 0.01$, $***P < 0.001$, ns indicates no significant difference. Scale bars = 1 mm in (a, b); 20 μm in (c–h).

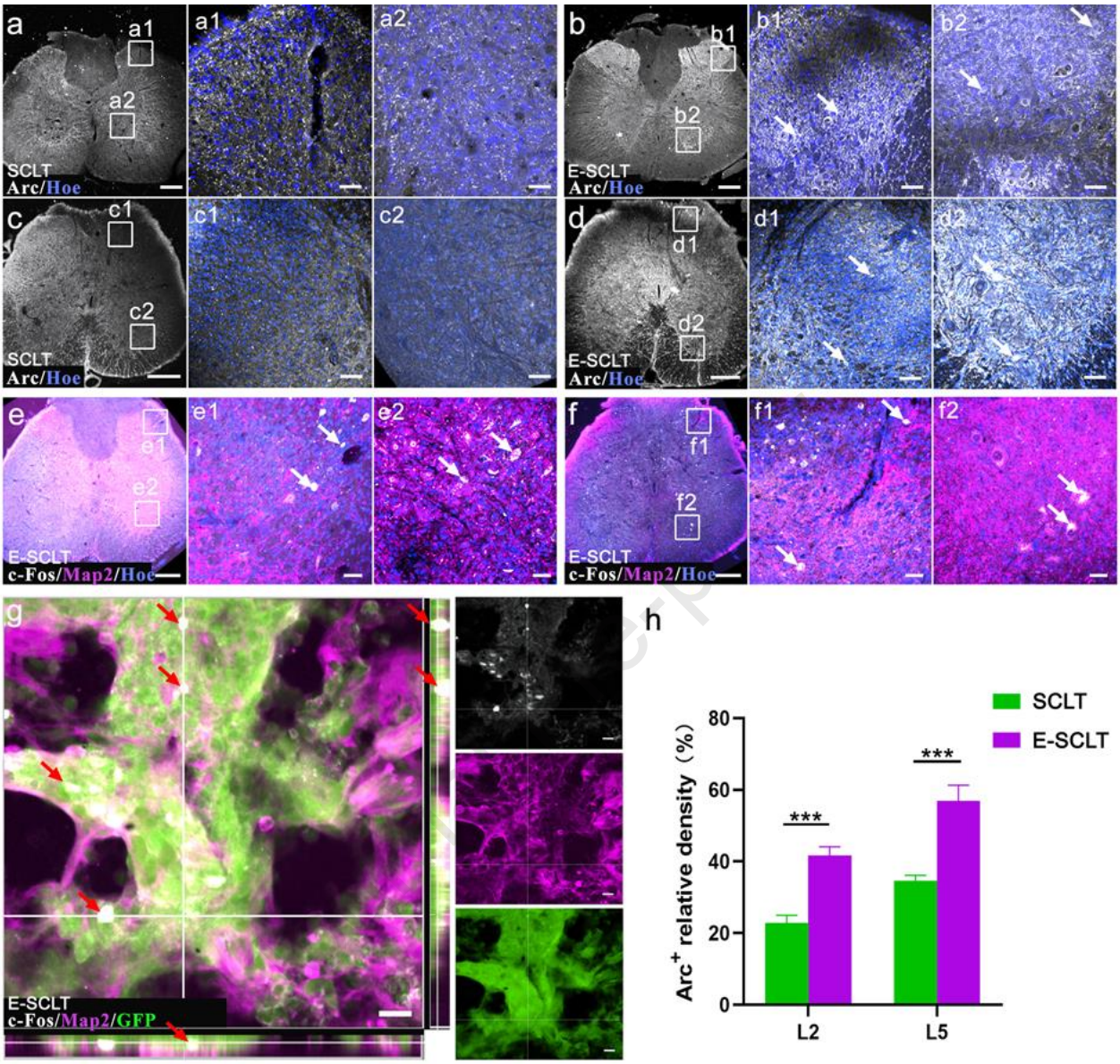
a
a1
a2
SCLT
Arc/Hoe
a1
a2
b
b1
b2
E-SCLT
Arc/Hoe
b1
b2
c
c1
c2
SCLT
Arc/Hoe
c1
c2
d
d1
d2
E-SCLT
Arc/Hoe
d1
d2
e
e1
e2
E-SCLT
c-Fos/Map2/Hoe
e1
e2
f
f1
f2
E-SCLT
c-Fos/Map2/Hoe
f1
f2
g
E-SCLT
c-Fos/Map2/GFP
h
SCLT
E-SCLT
Arc+ relative density (%)
80
60
40
20
0
***
***
L2
L5
i
SCI
E-SCI
SCLT
E-SCLT
Nor
PSD95
ChAT
SYP
NT-3
GAPHD
95kDa
68kDa
38kDa
27kDa
38kDa
j
SCI
E-SCI
SCLT
E-SCLT
Nor
Relative intensity
1.5
1.0
0.5
0.0
PSD95
ChAT
SYP
NT-3
***
***
**
*
ns
***
**
*
ns
***
**
*
ns
**
*

Fig. 4. Expression of neuron activation-related proteins in lumbar segment of spinal cord. a–b2) Arc^+ cells (arrows) scattered on an L2 transverse section in the SCLT (a) and E-SCLT (b) groups. c–d2) Arc^+ cells (arrows) scattered on an L5 transverse section in the SCLT (c) and E-SCLT (d) groups. e–f) c-Fos^+ neurons (arrows) in L2 and L5 transverse sections in the E-SCLT group; g) c-Fos^+/$Map2^+$/ GFP^+ cells (arrows) in the injury/graft site in the E-SCLT groups. h) Relative density of Arc^+ cells in the L2 and L5 (***$P < 0.001$). i) Western blot displaying bands of PSD95, ChAT, SYP, and NT-3 in the lumbar spinal cord . j) Bar chart showing the ratios of PSD95, ChAT, SYP, and NT-3 protein levels (*$P < 0.05$, **$P < 0.01$, ***$P < 0.001$). All the inserts are the higher magnification of boxed areas, showing the posterior and anterior horns. Scale bars = 300 μm in (a–f); 50 μm in (a1–f1), (a2–f2); 25 μm in (g).

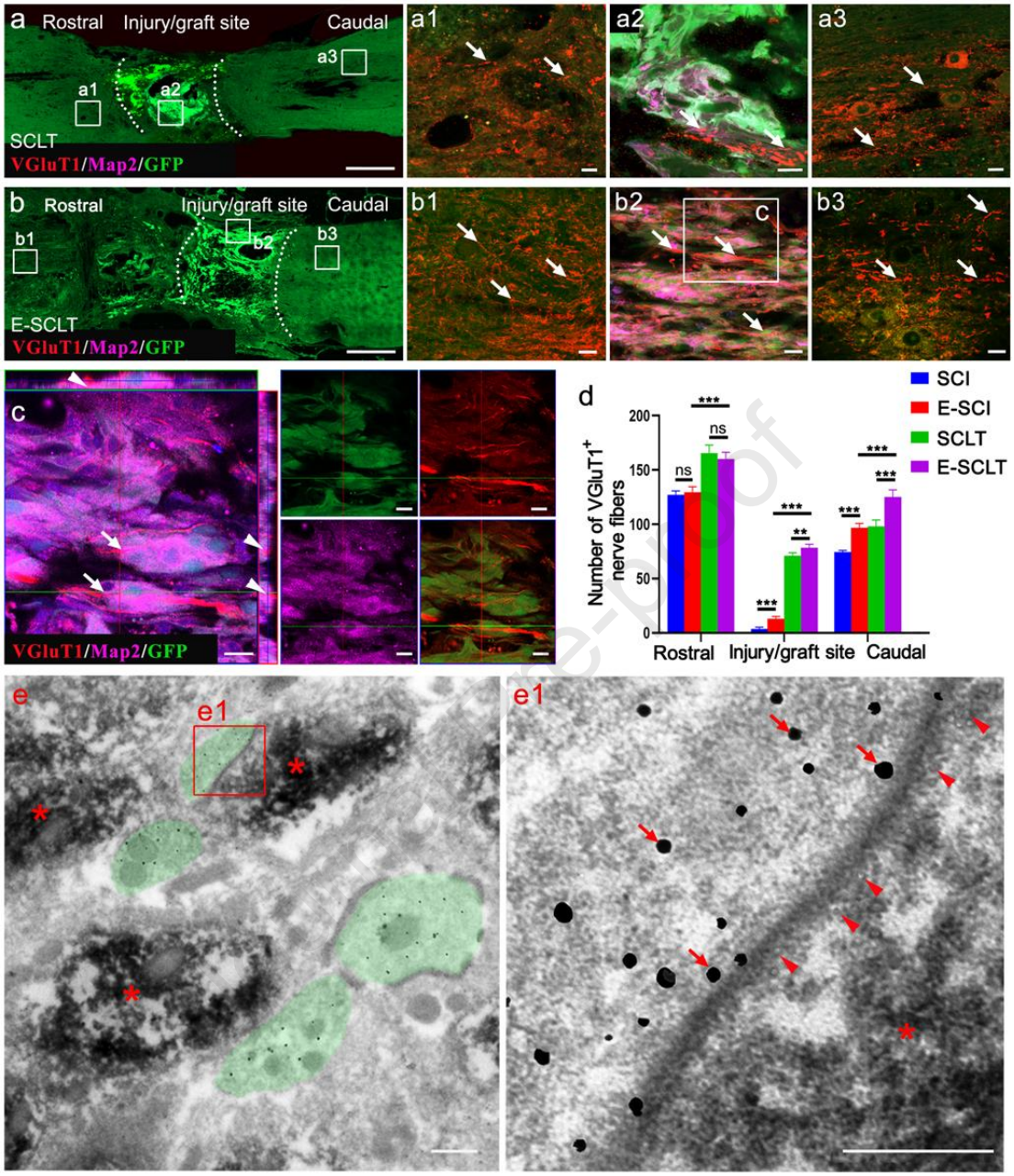

Fig. 5. Assessment of VGluT1$^+$ nerve fiber regeneration. a) VGluT1$^+$ nerve fibers in the region rostral to (a1), in (a2), and caudal to (a3) the injury/graft site in the SCLT group (arrows). b) VGluT1$^+$ nerve fibers in the region rostral to (b1), in (b2), and caudal to (b3) the injury/graft site in the E-SCLT group (arrows). c) VGluT1$^+$ nerve fibers (arrows) in close contact with Map2$^+$/GFP$^+$ neurons (arrowheads). d) Bar chart showing the number of VGluT1$^+$ nerve fibers in the regions rostral and caudal to/in the injury/graft site (*P < 0.05, **P < 0.01, ***P < 0.001; ns indicates no significant difference). e, e1) IEM of VGluT1$^+$ nerve fibers (labeled with DAB,

asterisks) distributed in neuropil in the injury/graft site; higher magnification of the boxed area in (d) showed a VGluT1^{+} nerve fiber in close contact with the GFP^{+} cell structure (labeled by nanogold particles, arrows) to form a synapse-like structure (d1). Scale bars = 500 μm in (D,E,H,I); 20 μm in (a–-a3), (b1–b3); 10 μm in (c); 1 μm in (e); 500 nm in (e1).

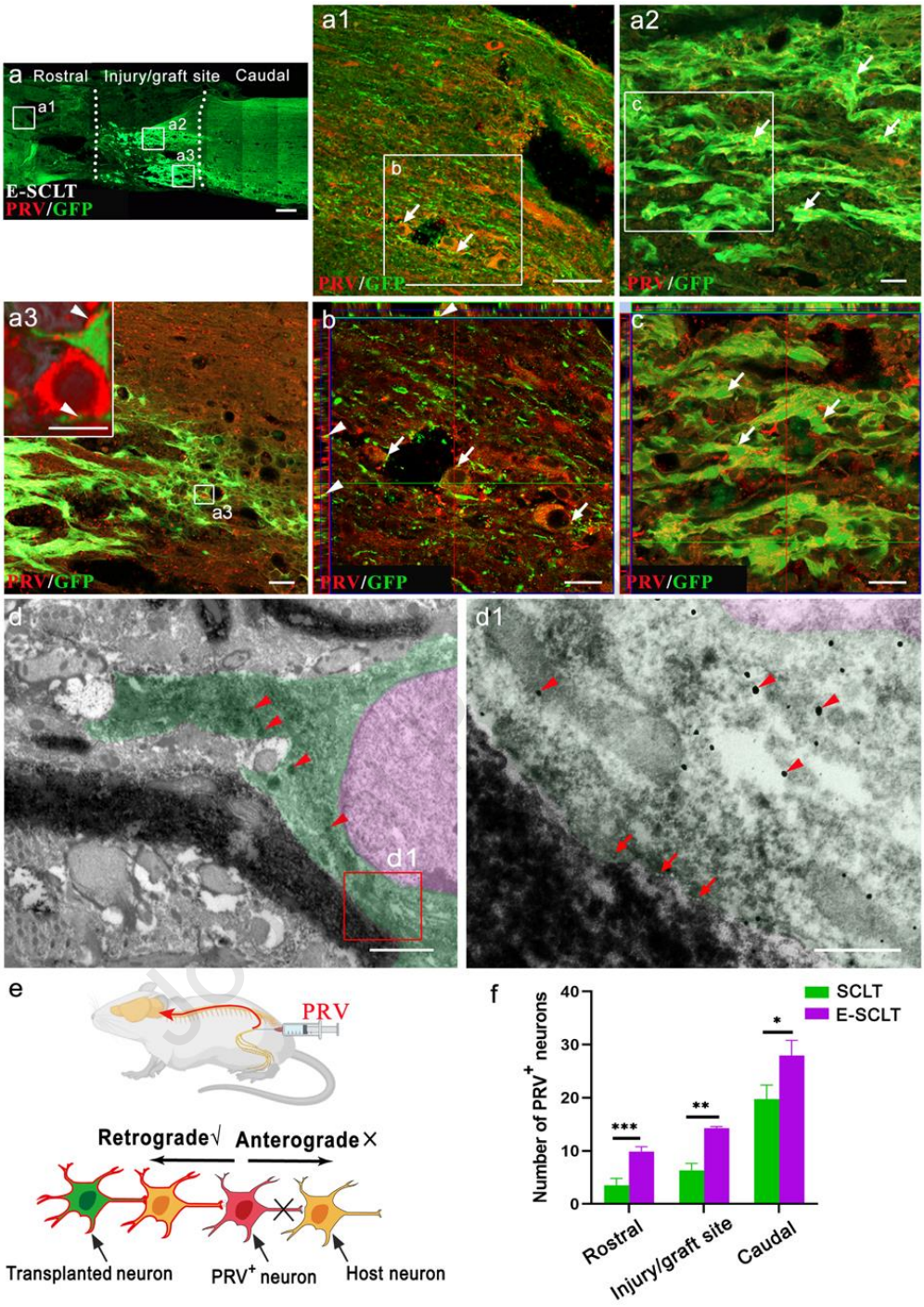

Fig. 6. Assessment of PRV$^+$ neuron distribution. a) Lower magnification of sagittal spinal cord sections in the E-SCLT group. a1–a3) Representative images showing the rostral region (a1) to/in the injury/graft site (a2, a3). b) Higher magnification of PRV$^+$ host neurons (arrows) contacting GFP$^+$ cell processes (arrowheads) in the rostral region (a1). c) Boxed area from the injury/graft site (a2) showing PRV$^+$/GFP$^+$ cells (arrows). d, d1) IEM of PRV$^+$ nerve fibers (DAB

staining) around a GFP^+ cell (with a pseudocolored purple nucleus and green cytoplasm in d), one in close contact with the GFP^+ cell (nanogold particle staining, arrowheads) to form a synapse-like structure (arrows, in d1). The cytoplasm of the GFP^+ cell also contained DAB-stained PRV^+ clusters (arrowheads in d). e) Schematic diagram showing the injection site (sciatic nerve) and retrograde transmission of PRV. f) Bar chart showing the number of PRV^+ neurons in the regions rostral and caudal to/in the injury/graft site (*P < 0.05, **P < 0.01, ***P < 0.001; ns indicates no significant difference). Scale bars = 500 μm in (a); 50 μm in (a1–a3); 10 μm in the white frame in (a3); 20μm in (b, c); 2 μm in (d); 1 μm in (d1).

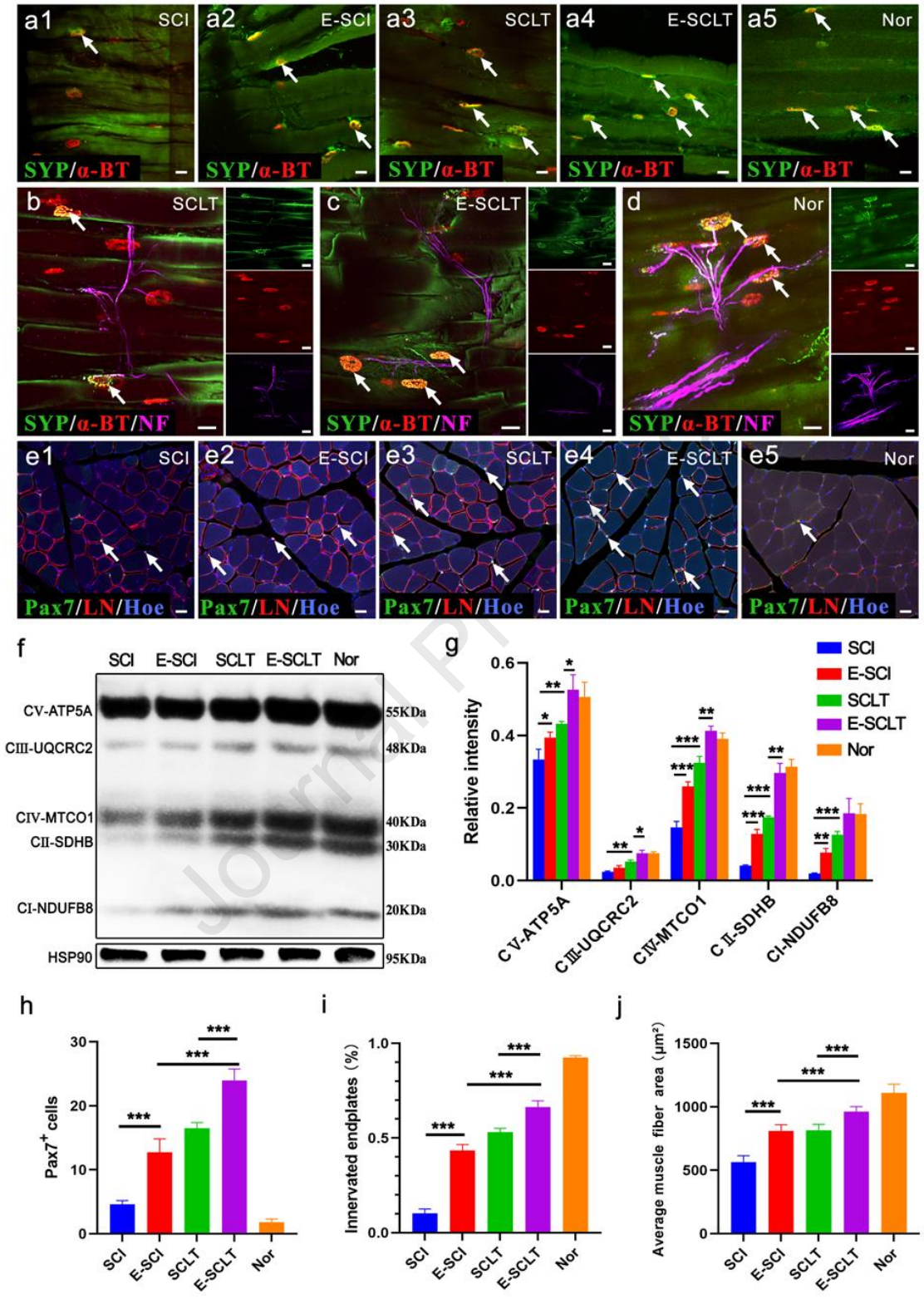

Fig. 7. Motor endplate, muscle stem cell, and muscle energy metabolism in the paralysis hindlimbs. a1–a5) Representative images displaying gastrocnemius muscle fiber $SYP^{+}/\alpha\text{-}BT^{+}$

motor endplates (arrows) in all groups. b–d) α-BT$^+$ motor endplates with SYP$^+$/NF$^+$ nerve fibers (arrows) in the SCLT, E-SCLT, and Nor groups. e1–e5) Representative images showing Pax7$^+$ cells (arrows) and laminin (LN)$^+$ extracellular matrix located between tibialis anterior muscle fibers in all groups. f) Western blot displaying bands of gastrocnemius mitochondrial respiratory chain complex proteins. g) Bar chart showing mitochondrial respiratory chain complex protein level ratios in all groups. h) Bar chart showing the ratio of SYP$^+$/α-BT$^+$ motor endplates to total α-BT$^+$ motor endplates. i) Bar chart showing the number of Pax7$^+$ cells per high power field (200×) in the tibialis anterior. j) Bar chart showing the average area per muscle fiber in the tibialis anterior. *P < 0.05, **P < 0.01, ***P < 0.001. Scale bars = 20 μm in (a1–a5, e1-e5); 50 μm in (b–d).

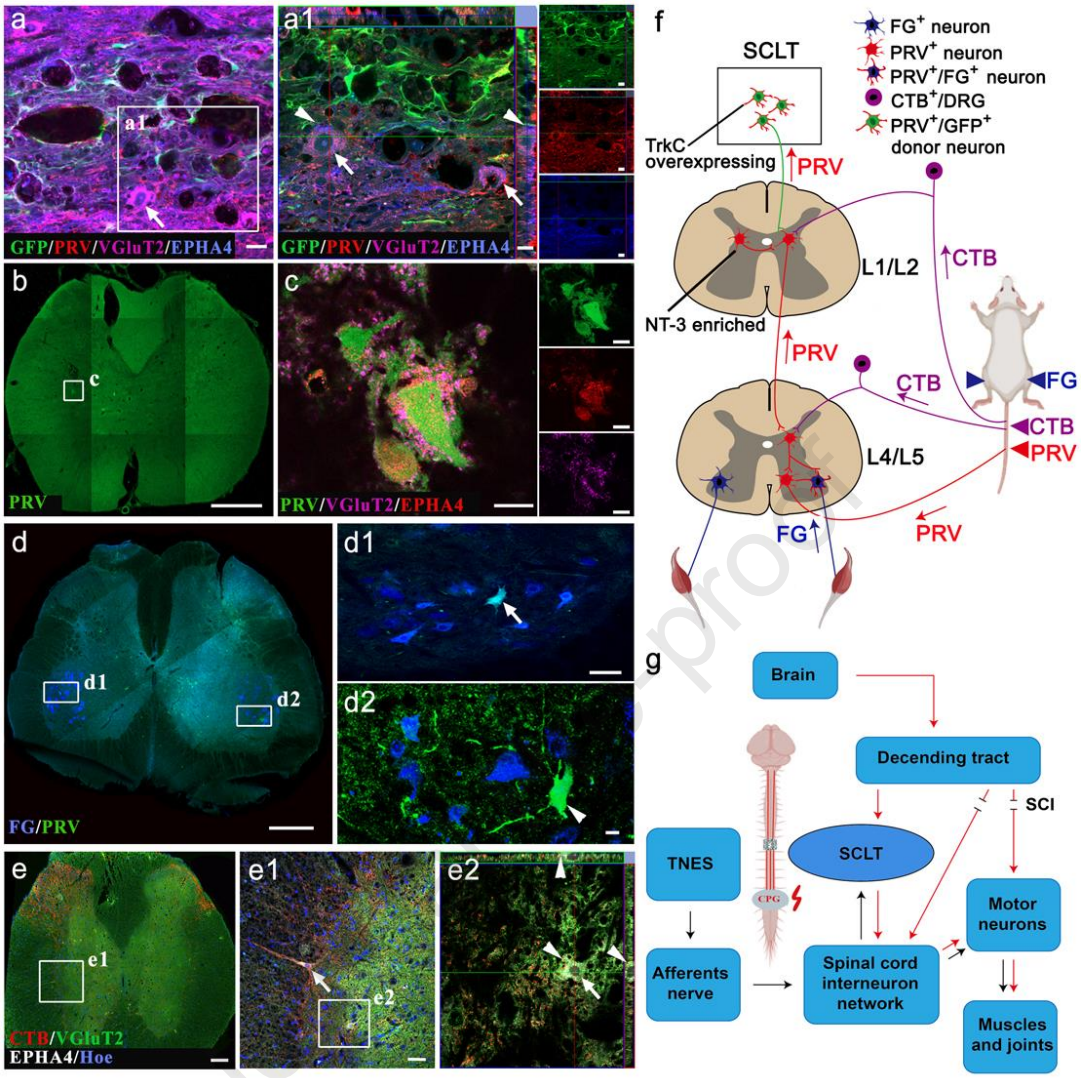

Fig. 8. Retrograde tracing neuronal connections in lower thoracolumbar spinal cord in the E-SCLT group. a, a1) PRV$^+$/EPHA4$^+$/VGluT2$^+$ CPG neurons (arrows) contacting GFP$^+$ donor cells (arrowheads) in the caudal region to the injury/graft site. b, c) Lower magnification of an L2 transverse section (b) of PRV$^+$ and higher magnification of the boxed area in (b) demonstrating a typical multipolar PRV$^+$/EPHA4$^+$/VGluT2$^+$ CPG neuron (c). d–d2) Lower magnification showing an L4 transverse section (d) FG$^+$/PRV$^+$ and higher magnification of the boxed area in (d), showing an FG$^+$/PRV$^+$ neuron (d1) and another FG$^+$ and PRV$^+$ neuron (d2). e) CTB$^+$ afferent nerve fibers in the L2 posterior horn. e1, e2) CTB$^+$ afferent nerve (arrowheads) contacting EPHA4$^+$/VGluT2$^+$ CPG neurons (arrows) in the L2 segment. f) Schematic diagram of the retrograde tracing of the sciatic nerve and tail nerve to uncover the pathway that TNES activates CPG neural circuits. g) Illustrated mechanism of combined TNES and SCLT effects (direction of the information, afferent

from TNES and descending from the brain, is indicated with black and red arrows, respectively). Scale bars = 20 μm in (a, c, d2); 10 μm in (a1); 500 μm in (b, d); 200 μm in (e); 50 μm in (d1, e1).

Declaration of interests

☒ The authors declare that they have no known competing financial interests or personal relationships that could have appeared to influence the work reported in this paper.

☐ The authors declare the following financial interests/personal relationships which may be considered as potential competing interests: